INTERNATIONAL JOURNAL FOR NUMERICAL METHODS IN FLUIDS
Int. J. Numer. Meth. Fluids 2001; **35**: 829–867

A fully non-linear model for three-dimensional overturning waves over an arbitrary bottom

Stéphan T. Grilli[a,*,1], Philippe Guyenne[b,2] and Frédéric Dias[c,3]

[a] *Ocean Engineering Department, University of Rhode Island, Narragansett, RI, U.S.A.*
[b] *Institut Non-Linéaire de Nice, UMR 6618 CNRS-UNSA, Valbonne, France*
[c] *Ecole Normale Supérieure, CMLA, UMR8536 CNRS, Cachan Cedex, France*

SUMMARY

An accurate three-dimensional numerical model, applicable to strongly non-linear waves, is proposed. The model solves fully non-linear potential flow equations with a free surface using a higher-order three-dimensional boundary element method (BEM) and a mixed Eulerian–Lagrangian time updating, based on second-order explicit Taylor series expansions with adaptive time steps. The model is applicable to non-linear wave transformations from deep to shallow water over complex bottom topography up to overturning and breaking. Arbitrary waves can be generated in the model, and reflective or absorbing boundary conditions specified on lateral boundaries. In the BEM, boundary geometry and field variables are represented by 16-node cubic 'sliding' quadrilateral elements, providing local inter-element continuity of the first and second derivatives. Accurate and efficient numerical integrations are developed for these elements. Discretized boundary conditions at intersections (corner/edges) between the free surface or the bottom and lateral boundaries are well-posed in all cases of mixed boundary conditions. Higher-order tangential derivatives, required for the time updating, are calculated in a local curvilinear co-ordinate system, using 25-node 'sliding' fourth-order quadrilateral elements. Very high accuracy is achieved in the model for mass and energy conservation. No smoothing of the solution is required, but regridding to a higher resolution can be specified at any time over selected areas of the free surface. Applications are presented for the propagation of numerically exact solitary waves. Model properties of accuracy and convergence with a refined spatio-temporal discretization are assessed by propagating such a wave over constant depth. The shoaling of solitary waves up to overturning is then calculated over a 1:15 plane slope, and results show good agreement with a two-dimensional solution proposed earlier. Finally, three-dimensional overturning waves are generated over a 1:15 sloping bottom having a ridge in the middle, thus focusing wave energy. The node regridding method is used to refine the discretization around the overturning wave. Convergence of the solution with grid size is also verified for this case.

KEY WORDS: boundary element method; breaking ocean waves; non-linear surface waves; numerical wave tank; potential flow; three-dimensional flows

* Correspondence to: Ocean Engineering Department, University of Rhode Island, Narragansett, RI 02882, U.S.A. Fax: +1 401 8746837.
[1] E-mail: grilli@oce.uri.edu
[2] E-mail: guyenne@inln.cnrs.fr
[3] E-mail: dias@cmla.ens-cachan.fr

Received July 1999
Revised June 2000

1. INTRODUCTION

Over the past two decades, the development of increasingly accurate and efficient numerical models of highly non-linear surface waves has been a continuous challenge in the ocean and coastal engineering and science communities. Indeed, wave dynamics govern most physical processes occurring (e.g., air–sea interactions, wave shoaling and breaking, wave-induced coastal currents, surf-zone dynamics, . . .), and engineering design methods used (e.g., for breaking wave impact pressures on coastal and off-shore structures, . . .) in these areas.

When dealing with waves prior to breaking, the most successful methods, whether theoretical or numerical, have been based on *potential flow theory*, which neglects both viscous and rotational effects on the wave flow. The governing equation in this case—the continuity equation—is a Laplace's equation for the potential. This linear partial differential equation (PDE) can efficiently be solved in a boundary integral equation (BIE) formulation, using either a free space or a more specialized Green's function; or by eigenfunction or polynomial expansions. Non-linear terms are included in the dynamic and kinematic free surface boundary conditions for the potential, and methods usually differ in accuracy, range of applicability, and numerical efficiency by the way they deal with these terms.

A traditional approach in most wave theories and numerical models based on these has been to define so-called small parameters (e.g., wave steepness, ratio of water depth to wavelength, . . .) and to express truncated series expansions of free surface boundary conditions and geometry as a function of these parameters (see, e.g., Mei [1]). In this line, wave propagation models based on so-called extended higher-order Boussinesq equations have recently produced quite impressive results in coastal areas, for shallow and intermediate waters (e.g., Wei *et al.* [2]).

When dealing with strongly non-linear waves close to breaking or starting to break (i.e., overturning waves), methods based on small parameters and, in most cases, on a single-valued Eulerian description of the free surface, become irrelevant. For such cases, governing equations must be solved in their primitive form and the time integration must be based on a mixed Eulerian–Lagrangian (MEL) formulation following fluid particle trajectories on the free surface. Many such numerical solutions of potential flow theory (referred to as 'fully non-linear potential flow' (FNPF) problems) have been developed, mostly in two dimensions (2D), and have been shown to model the physics of wave overturning in deep and intermediate water (e.g., Dommermuth *et al.* [3] and Skyner [4]) and wave shoaling and breaking over slopes (e.g., Grilli *et al.* [5,6], Li and Raichlen [7]), with a surprising degree of accuracy. Let us mention for completion that recent improvements in computer power have also led to an increasing use of modernized volume of fluid (VOF) methods solving complete Navier–Stokes equations for free surface flows (e.g., Grilli [8], Guignard *et al.* [9]; Chen *et al.* [10]). Such VOF methods can model post-breaking waves, but they are computationally expensive, particularly in three dimensions (3D), and suffer from numerical diffusion leading to artificial loss of wave energy over long distances of propagation. Hence, in such cases, unless the post-breaking wave flow is the focus of the study, FNPF theory, which is more accurate and efficient, is preferred over VOF methods. A promising recent development is the coupling of

FNPF and VOF methods for pre- and post-breaking wave flows respectively (Guignard *et al.* [11]).

Thus, most studies to date dealing with transformations of waves leading to breaking have been based on an FNPF formulation. Furthermore, in most FNPF models, Laplace's equation has been solved with a higher-order boundary element method (BEM; Brebbia [12]), either based on Green's identity or on Cauchy integral theorem formulations. Time integration of free surface boundary conditions (expressed in an MEL formulation) has been performed either using a time marching (Runge–Kutta) or a predictor–corrector (Adams–Bashforth–Moulton) scheme, or both (e.g., Longuet-Higgins and Cokelet [13]), or a Taylor series expansion method (Dold and Peregrine [14]). Early computations following this approach were two-dimensional and restricted to space–periodic waves over constant depth [13–16], but more recent two-dimensional models can accommodate both arbitrary incident waves and complex bottom topographies (e.g., Klopman [17], Grilli *et al.* [18], Cointe [19], Cooker [20], and Ohyama and Nadaoka [21]). Most recent models also directly work in a physical space region, i.e., in a *numerical wave tank* (NWT), in which incident waves are generated at one extremity and reflected, absorbed, or radiated at the other extremity (see Grilli and Subramanya [22] and Grilli and Horrillo [23] for details).

Three-dimensionality, in addition to producing quite formidable numerical problems, poses more difficult geometric and far-field representation problems than two-dimensionality. In naval hydrodynamics and offshore engineering fields many authors have proposed (mostly BEM based but often with constant panels) three-dimensional models for weakly and, more recently, fully non-linear permanent or transient wave patterns created by submerged sources, or submerged/floating bodies moving at constant or variable speed (e.g., Dommermuth and Yue [24], Forbes [25], Boo [26], and Lee *et al.* [27]), or transient wave diffraction, run-up, and forces on surface piercing cylinders (e.g., Isaacson [28], Yang and Ertekin [29], Cheung *et al.* [30], Lalli *et al.* [31], Celebi *et al.* [32], and Ferrant [33]). In these problems, the free surface is always single-valued and, by assuming infinite or constant depth (image method) and open ocean, the problem often reduces to only discretizing the free surface and the body.

Only a few attempts have been reported of solving FNPF problems for transient non-linear wave propagation in general 3D-NWTs, two of them modeling overturning waves. Romate [34] developed a three-dimensional (constant) panel method, which he applied to weakly non-linear waves generated by a wavemaker and propagating in a narrow 3D-NWT. His time stepping method was similar to that in Reference [13] but results were quite limited and affected by spurious waves, maybe due to problems at intersections between the free surface and lateral boundaries. Xü and Yue [35,36] calculated three-dimensional overturning waves in a doubly-periodic computational domain with infinite depth (i.e., only the free surface was discretized). They used a higher-order BEM based on Green's identity, with a doubly periodic Green's function in the x- and y-directions, quadratic isoparametric boundary elements, and an MEL time stepping similar to that of Reference [13]. As in the two-dimensional solution of Reference [13], sawtooth instabilities eventually developed near wave crests; these were eliminated by smoothing, typically applied every few time steps. As in Reference [13], initially two-dimensional periodic waves were made to break by specifying an asymmetric surface pressure. Broeze [37] developed a method similar to Xü and Yue's and was able to produce the

initial stages of overturning waves over a bottom obstacle; numerical instabilities were also experienced, which limited computations. Boo *et al.* [38] produced irregular non-linear waves in a 3D-NWT; they used a higher-order BEM and a semi-Lagrangian time marching scheme similar to that in Reference [13]. Sawtooth instabilities occurred and were eliminated by smoothing. Ferrant [33,39] developed a 3D-NWT based on a BEM with linear elements, and an MEL time stepping similar to that of Reference [13]. He studied wave radiation–diffraction by floating bodies and wave forces on surface piercing cylinders; an annular absorbing beach was used at the exterior boundary. Note that, in the previous two studies, BEM matrices were maintained constant for several time steps in order to save on computational time. Celebi *et al.* [32] studied diffraction of periodic waves around bottom mounted columns, using a BEM with an MEL time stepping, in an NWT having both wave generation and absorbing beach boundaries.

Reviews of two- and three-dimensional highly non-linear wave problems to date can be found in Romate [34], Yeung [40], Peregrine [41], Grilli [42], Grilli and Subramanya [43], Tsai and Yue [44], and Kim *et al.* [45].

From the above it appears that FNPF theory can be used to model overturning waves over an arbitrary bottom. Many such two-dimensional and a few three-dimensional solutions (i.e., NWTs) have been proposed. Among these, the most stable and accurate models were those in which higher-order spatial and temporal discretizations methods were used, and important problems such as corner/edge boundary conditions and numerical integrations were carefully addressed. Importantly, in the few existing higher-order two-dimensional models [14,18,22], strongly non-linear waves were accurately propagated over long distances and/or time, up to overturning, without the need for smoothing or filtering of the solution. The non-linear nature of the problem and lack of dissipation in FNPF theory indeed are such that numerical errors, even very small, remain an integral part of the solution and build up as a function of time through superposition and non-linear interactions. Therefore, such errors must be minimized by seeking optimum accuracy in all numerical aspects of the model.

In the present study, the experience gained by the authors in developing accurate and stable numerical methods for 2D-FNPF-NWTs is applied to the development of a new, similarly accurate, 3D-FNPF-NWT for strongly non-linear waves. The model is developed using a higher-order 3D-BEM and an MEL time updating, based on a second-order Taylor series expansion, with adaptive time steps, similar to that used in the two-dimensional model of Reference [18]. The model is applicable to non-linear wave transformations up to overturning and breaking, from deep to shallow water over arbitrary bottom topography. Arbitrary waves can be generated in the NWT by wavemakers or directly on the free surface (note only the latter method will be detailed here). Reflective and absorbing boundary conditions are implemented on lateral boundaries of the NWT; for the latter in a way similar to Grilli and Horrillo [23] (note no application of absorbing boundaries will be presented here). Geometry and field variables are represented on the NWT boundary by 16-node cubic 'sliding' two-dimensional elements similar, in principle, to the one-dimensional 4-node 'middle-interval-interpolation (MII)' elements introduced by Grilli and Subramanya [22] in their two-dimensional model. Such elements provide local inter-element continuity of the first and second derivatives. Accurate and efficient numerical integrations are developed for these elements. Discretized boundary conditions at intersections (corner/edges) between the free

surface or the bottom and lateral boundaries are well-posed in all cases of mixed boundary conditions following the methods introduced by Grilli and Subramanya [22] and Grilli and Svendsen [46]. Higher-order tangential derivatives required for the time updating are calculated in a local curvilinear co-ordinate system using two-dimensional 25-node sliding fourth-order elements similar in principle to the 5-node one-dimensional elements introduced by Grilli and Svendsen [46] for calculating s-derivatives in their two-dimensional model. Node regridding to a higher resolution can be specified over selected areas of the free surface. Details of the model development and implementation are given in Section 2 and applications are presented in Section 3. These are first aimed at assessing the model properties of accuracy and convergence with a refined spatio-temporal discretization, by checking errors on conservation of mass and energy for solitary wave propagation over constant depth. The shoaling of solitary waves up to breaking is then calculated over a 1:15 plane slope in a quasi-two-dimensional configuration and results are compared with two-dimensional results by Grilli *et al.* [6]. Finally, three-dimensional overturning waves are calculated over a 1:15 sloping bottom having a ridge in the middle, thus focusing wave energy. The node regridding method is tested in the latter application and convergence of results with grid size is verified.

2. THE MATHEMATICAL AND NUMERICAL MODEL

2.1. Governing equations and boundary conditions

Equations for fully non-linear potential flows with a free surface are listed in the following. The velocity potential $\phi(\boldsymbol{x}, t)$ is used to represent inviscid irrotational three-dimensional flows in Cartesian co-ordinates (x, y, z), with z the vertical upward direction (and $z = 0$ at the undisturbed free surface). The velocity is defined by (Figure 1)

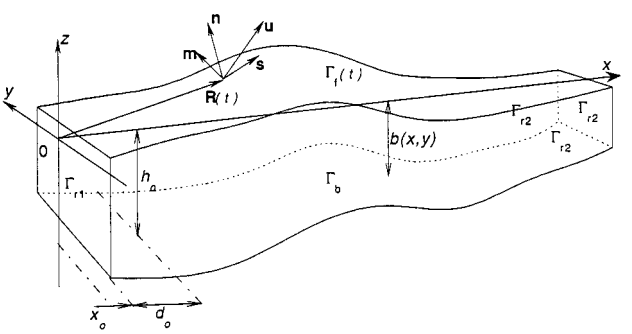

Figure 1. Sketch of computational domain for 3D-BEM solution of FNPF equations. The domain is defined for $x \geq x_0$. Note a region of constant depth $h = h_0$ is specified for $x \leq x_0 + d_0$, beyond which depth is set to $h = b(x, y)$. Tangential vectors at point $\boldsymbol{R}(t)$ of the free surface $\Gamma_f(t)$ are defined as $(\boldsymbol{s}, \boldsymbol{m})$ and outward normal vector as $\boldsymbol{n}$.

$$\boldsymbol{u} = \nabla\phi = (u, v, w) \tag{1}$$

The continuity equation in the fluid domain $\Omega(t)$, with boundary $\Gamma(t)$, is a Laplace equation for the potential

$$\nabla^2\phi = 0, \quad \text{in } \Omega(t) \tag{2}$$

The corresponding three-dimensional free space Green's function is defined as (e.g., Brebbia [12])

$$G(\boldsymbol{x}, \boldsymbol{x}_l) = \frac{1}{4\pi r}, \quad \text{with } \frac{\partial G}{\partial n}(\boldsymbol{x}, \boldsymbol{x}_l) = -\frac{1}{4\pi}\frac{\boldsymbol{r}\cdot\boldsymbol{n}}{r^3} \tag{3}$$

and

$$\boldsymbol{r} = \boldsymbol{x} - \boldsymbol{x}_l \tag{4}$$

with $r = |\boldsymbol{r}|$ being the distance from point $\boldsymbol{x} \equiv (x, y, z)$ to the reference point $\boldsymbol{x}_l \equiv (x_l, y_l, z_l)$, both being on boundary Γ, and $\boldsymbol{n}$ representing the outward normal unit vector to the boundary at point $\boldsymbol{x}$.

Green's second identity transforms Equation (2) into the BIE

$$\alpha(\boldsymbol{x}_l)\phi(\boldsymbol{x}_l) = \int_{\Gamma(\boldsymbol{x})} \left\{ \frac{\partial\phi}{\partial n}(\boldsymbol{x}) G(\boldsymbol{x}, \boldsymbol{x}_l) - \phi(\boldsymbol{x}) \frac{\partial G}{\partial n}(\boldsymbol{x}, \boldsymbol{x}_l) \right\} \mathrm{d}\Gamma \tag{5}$$

in which $\alpha(\boldsymbol{x}_l) = \theta_l/(4\pi)$, with θ_l the exterior solid angle made by the boundary at point $\boldsymbol{x}_l$ (i.e., 2π for a smooth boundary; Brebbia [12]).

Boundary Γ is divided into various parts with different boundary conditions (Figure 1). On the free surface $\Gamma_f(t)$, ϕ satisfies the non-linear kinematic and dynamic boundary conditions

$$\frac{\mathrm{D}\boldsymbol{R}}{\mathrm{D}t} = \boldsymbol{u} = \nabla\phi \quad \text{on } \Gamma_f(t) \tag{6}$$

$$\frac{\mathrm{D}\phi}{\mathrm{D}t} = -gz + \frac{1}{2}\nabla\phi\cdot\nabla\phi - \frac{p_a}{\rho} \quad \text{on } \Gamma_f(t) \tag{7}$$

respectively, with $\boldsymbol{R}$ the position vector of a free surface fluid particle, g the acceleration due to gravity, p_a the atmospheric pressure, ρ the fluid density, and the material derivative being defined as

$$\frac{\mathrm{D}}{\mathrm{D}t} \equiv \frac{\partial}{\partial t} + \boldsymbol{u}\cdot\nabla \tag{8}$$

Various methods can be used for wave generation in the model (Grilli *et al.* [23,46]). For instance, when waves are generated by simulating a wavemaker motion on the 'open sea' boundary of the computational domain, $\Gamma_{r1}(t)$, motion and velocity $[\boldsymbol{x}_p, \boldsymbol{u}_p]$ are specified over the wavemaker as

$$\bar{\boldsymbol{x}} = \boldsymbol{x}_p \quad \text{and} \quad \overline{\frac{\partial \phi}{\partial n}} = \boldsymbol{u}_p \cdot \boldsymbol{n} \quad \text{on } \Gamma_{r1}(t) \tag{9}$$

where overlines denote specified values.

Along the bottom Γ_b and other stationary parts of the boundary, referred to as Γ_{r2}, a no-flow condition is prescribed as

$$\overline{\frac{\partial \phi}{\partial n}} = 0, \quad \text{on } \Gamma_b \quad \text{and} \quad \Gamma_{r2} \tag{10}$$

Note $\Gamma \equiv \Gamma_f \cup \Gamma_{r1} \cup \Gamma_{r2} \cup \Gamma_b$.

2.2. Time integration

Free surface boundary conditions (6) and (7) are integrated at time t to establish both the new position and the boundary conditions on the free surface $\Gamma_f(t)$ at a subsequent time $(t + \Delta t)$ (with Δt a varying time step).

Following the method implemented in Grilli *et al.*'s [18,22] two-dimensional model, second-order explicit Taylor series expansions are used to express both the new position $\boldsymbol{R}(t + \Delta t)$ and the potential $\phi(\boldsymbol{R}(t + \Delta t))$ on the free surface, in an Eulerian–Lagrangian formulation

$$\bar{\boldsymbol{R}}(t + \Delta t) = \boldsymbol{R}(t) + \Delta t \frac{\mathrm{D}\boldsymbol{R}}{\mathrm{D}t}(t) + \frac{(\Delta t)^2}{2} \frac{\mathrm{D}^2 \boldsymbol{R}}{\mathrm{D}t^2}(t) + \mathcal{O}[(\Delta t)^3] \tag{11}$$

$$\bar{\phi}(\boldsymbol{R}(t + \Delta t)) = \phi(t) + \Delta t \frac{\mathrm{D}\phi}{\mathrm{D}t}(t) + \frac{(\Delta t)^2}{2} \frac{\mathrm{D}^2 \phi}{\mathrm{D}t^2}(t) + \mathcal{O}[(\Delta t)^3] \tag{12}$$

Coefficients in these Taylor series are expressed as functions of the potential, its partial time derivative, and the normal and tangential derivatives of both of these along the free surface (details of calculations of tangential derivatives are given in a following section).

More specifically, first-order coefficients are given by Equations (6) and (7), which requires calculating $(\phi, \partial\phi/\partial n)$ on the free surface. This is done by solving the BIE (5) at time t, with boundary conditions (9), (10), and (12) (see next section). Second-order coefficients are obtained from the material derivative of Equations (6) and (7), which requires also calculating $(\partial\phi/\partial t, \partial^2\phi/\partial t\, \partial n)$ at time t; this is done by solving a BIE similar to Equation (5) for these fields. The free surface boundary condition for this second BIE is obtained from the Bernoulli equation (7) after solution of the first BIE for ϕ as

$$\overline{\frac{\partial \phi}{\partial t}} = -gz - \frac{1}{2}\nabla\phi\cdot\nabla\phi - \frac{p_a}{\rho}, \quad \text{on } \Gamma_f(t) \tag{13}$$

For a wave generation by a wavemaker, Equation (9) gives

$$\overline{\frac{\partial^2 \phi}{\partial t\,\partial n}} = \frac{\partial(\boldsymbol{u}_p\cdot\boldsymbol{n})}{\partial t}, \quad \text{on } \Gamma_{r1}(t) \tag{14}$$

and for the bottom and other stationary boundaries

$$\overline{\frac{\partial^2 \phi}{\partial t\,\partial n}} = 0 \quad \text{on } \Gamma_b \text{ and } \Gamma_{r2} \tag{15}$$

Note that the BIEs for ϕ and $\partial\phi/\partial t$ are solved at time t and thus both correspond to the same boundary geometry and have the same discretized form (see next section). Therefore, the solution of the second BIE only takes a small fraction of the time (typically a few per cent) needed for the solution of the first BIE (when using a direct method of solution). This makes this time stepping method very efficient, particularly when compared with higher-order Runge–Kutta or Adams–Bashforth–Moulton schemes used in other studies (e.g., Longuet-Higgins and Cokelet [13], Romate [34]) which often require multiple evaluations of the BIE (5) for several intermediate times per time step. Other advantages of this time stepping scheme are of being explicit and using spatial derivatives of the field variables along the free surface in the calculation of values at $(t+\Delta t)$. This provides more stability to the computed solution and makes it possible to use larger time steps with a similar accuracy, thus making the overall solution more efficient.

2.3. Boundary discretization

2.3.1. Classical BEM. The BIE (5) for ϕ, and its equivalent for $\partial\phi/\partial t$, are solved by a BEM [12].

In this method, the boundary is discretized into N_Γ collocation nodes and M_Γ higher-order elements are used to define local interpolations in between m of these nodes. Thus, within the kth such element, Γ_e^k, both the boundary geometry and field variables (denoted by $u=\phi$ and $q=\partial\phi/\partial n$ for simplicity and generality) are discretized using shape functions. Here, shape functions are analytically defined, as higher-order polynomials, over a single reference element $\Gamma_{\xi,\eta}$, to which the M_Γ 'Cartesian' elements of arbitrary shape are transformed by a change of variable. The intrinsic co-ordinates on the reference element are denoted by $(\xi,\eta)\in[-1,1]$. Variations of the geometry and field variables over each element k are described by their nodal values, $\boldsymbol{x}_j^k$, u_j^k, and q_j^k, and by the local shape functions $N_j(\xi,\eta)$ as

$$\boldsymbol{x}(\xi,\eta) = N_j(\xi,\eta)\boldsymbol{x}_j^k \tag{16}$$

$$u(\xi,\eta) = N_j(\xi,\eta)u_j^k \quad \text{and} \quad q(\xi,\eta) = N_j(\xi,\eta)q_j^k \tag{17}$$

where $j = 1, \ldots, m$ locally numbers the nodes within each element Γ_e^k, for $k = 1, \ldots, M_\Gamma$, and the summation convention is applied to repeated subscripts.

The shape functions are selected as polynomials of (ξ, η), whose coefficients are found by requiring that $u(\xi, \eta)$ take the value u_i^k at node $\boldsymbol{x}_i^k$, i.e., in Equation (17)

$$u(\xi(\boldsymbol{x}_i^k), \eta(\boldsymbol{x}_i^k)) = N_j(\xi_i, \eta_i) u_j^k = u_i^k$$

Hence, for the ith node of an m-node reference element, shape functions must satisfy

$$N_j(\xi_i, \eta_i) = \delta_{ij} \quad \text{with } i, j = 1, \ldots, m \text{ on } \Gamma_{\xi,\eta} \tag{18}$$

and δ_{ij} is the Kronecker symbol. Values of (ξ_i, η_i) only depend on the element shape (i.e., triangular, quadrilateral) and degree (i.e., linear, quadratic). The solution of Equation (18) for selected element shape and degree thus provides corresponding closed form expressions for the shape functions (see next section). Note when the same shape functions are used for both the geometry and the field variables, one defines so-called isoparametric elements.

2.3.2. The 3D-MII method. Isoparametric elements can provide a high-order approximation within their area of definition but only offer C_0 continuity of the geometry and field variables at the common nodes in between elements.

Based on the experience acquired in two-dimensional problems, for such highly non-linear water wave problems one needs to define elements that are both higher-order within their area of definition and at least locally C_2 continuous in between elements. To do so, various methods, including cubic-spline-based elements, were used in two-dimensional models [22,46]. Here, elements are defined using an extension of the so-called MII method introduced by Grilli and Subramanya [22] in their two-dimensional model. Boundary elements are 4-node quadrilaterals with cubic shape functions defined using both these and additional neighboring nodes in each direction, for a total of $m = 16$ nodes. Hence, only part of the interval of variation (usually the middle part) of the cubic shape functions is used for calculating the boundary integrals in Equation (5) (Figure 2).

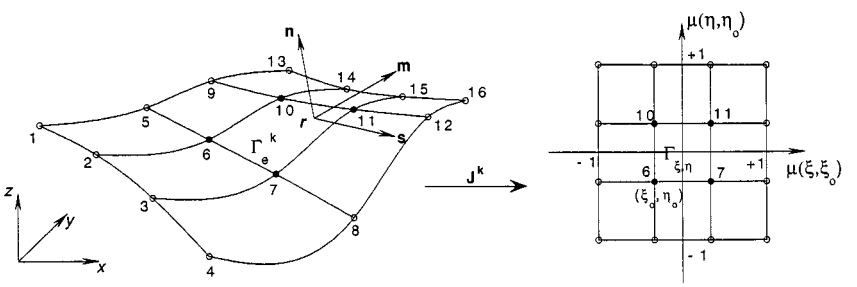

Figure 2. Sketch of 16-node cubic 3D-MII Cartesian element Γ_e^k and corresponding reference element $\Gamma_{\xi,\eta}$. Quadrilateral element nodes are indicated by symbols (●), and additional nodes by symbols (○). The curvilinear co-ordinate system ($\boldsymbol{s}$, $\boldsymbol{m}$, $\boldsymbol{n}$) has been marked at point $\boldsymbol{r}$ of the element. (ξ_0, η_0) marks the bottom left node of the quadrilateral, transformed as part of the reference element by $\mathbf{J}^k$.

In the present 3D-MII method, two-dimensional bi-cubic shape functions are defined on the reference element as the product of two one-dimensional cubic shape functions $N'_c(\mu)$, with $c = 1, \ldots, 4$ and $\mu \in [-1, 1]$, i.e.

$$N_j(\xi, \eta) = N'_{b(j)}(\mu(\xi, \xi_0))N'_{d(j)}(\mu(\eta, \eta_0)) \tag{19}$$

with b and $d = 1, \ldots, 4$; $j = 4(d-1) + b$, and property (18) implying

$$N'_c(\mu_i) = \delta_{ic} \quad \text{with} \quad \mu_i = \frac{2i-5}{3} \tag{20}$$

for $i = 1, \ldots, 4$. Hence, solving Equation (20)

$$N'_1(\mu) = \frac{1}{16}(1-\mu)(9\mu^2 - 1), \qquad N'_2(\mu) = \frac{9}{16}(1-\mu^2)(1-3\mu),$$

$$N'_3(\mu) = \frac{9}{16}(1-\mu^2)(1+3\mu), \qquad N'_4(\mu) = \frac{1}{16}(1+\mu)(9\mu^2 - 1) \tag{21}$$

For the MII method, the additional transformation from μ to the intrinsic coordinates (ξ, η) on the reference element is formally expressed as

$$\mu(\chi, \chi_0) = \chi_0 + \frac{1}{3}(1+\chi) \tag{22}$$

with $\chi = \xi$ or η and $\chi_0 = \xi_0$ or $\eta_0 = -1, -1/3$, or $1/3$, depending on which of the nine quadrilaterals defined by the $m = 16$ nodes is selected (Figure 2). Note this selection depends on the location of the element with respect to the intersections between various parts of the boundary (such as the free surface and lateral boundaries).

2.3.3. Discretized BIEs. Integrals in Equation (5) are transformed into a sum of integrals over the boundary elements, each of which is calculated within the reference element $\Gamma_{\xi,\eta}$. To do so, the curvilinear change of variables introduced above $[\boldsymbol{x} \to (\xi, \eta)]$ is expressed for element Γ_e^k by a Jacobian matrix $\mathbf{J}^k$ obtained as follows. Two orthogonal tangential vectors are defined at point $\boldsymbol{x}(\xi, \eta)$ of the boundary as (using Equations (17) and (18))

$$\frac{\partial \boldsymbol{x}}{\partial \xi} = \frac{\partial N_j(\xi, \eta)}{\partial \xi}\boldsymbol{x}_j^k = \left\{\frac{\partial N'_{b(j)}(\mu(\xi, \xi_0))}{\partial \mu}\frac{\partial \mu}{\partial \xi}N'_{d(j)}(\mu(\eta, \eta_0))\right\}\boldsymbol{x}_j^k,$$

$$\frac{\partial \boldsymbol{x}}{\partial \eta} = \frac{\partial N_j(\xi, \eta)}{\partial \eta}\boldsymbol{x}_j^k = \left\{N'_{b(j)}(\mu(\xi, \xi_0))\frac{\partial N'_{d(j)}(\mu(\eta, \eta_0))}{\partial \mu}\frac{\partial \mu}{\partial \eta}\right\}\boldsymbol{x}_j^k \tag{23}$$

with $j = 1, \ldots, m$ on Γ_e^k $(k = 1, \ldots, M_\Gamma)$ and from Equation (22)

$$\frac{\partial \mu}{\partial \xi} = \frac{\partial \mu}{\partial \eta} = \frac{1}{3}$$

Corresponding tangential unit vectors are further defined as

$$\boldsymbol{s}(\xi, \eta) = \frac{1}{h_1}\frac{\partial \boldsymbol{x}}{\partial \xi} \quad \text{and} \quad \boldsymbol{m}(\xi, \eta) = \frac{1}{h_2}\frac{\partial \boldsymbol{x}}{\partial \eta} \tag{24}$$

with the scale factors

$$h_1 = \left|\frac{\partial \boldsymbol{x}}{\partial \xi}\right| \quad \text{and} \quad h_2 = \left|\frac{\partial \boldsymbol{x}}{\partial \eta}\right| \tag{25}$$

A third vector is defined at the same point in the normal direction, as

$$\frac{\partial \boldsymbol{x}}{\partial \zeta} = \frac{\partial \boldsymbol{x}}{\partial \xi} \times \frac{\partial \boldsymbol{x}}{\partial \eta} \tag{26}$$

The corresponding unit normal vector is thus defined as

$$\boldsymbol{n}(\xi, \eta) = \frac{1}{h_1 h_2}\frac{\partial \boldsymbol{x}}{\partial \zeta} = \boldsymbol{s} \times \boldsymbol{m} \quad \text{with} \quad \left|\frac{\partial \boldsymbol{x}}{\partial \zeta}\right| = h_1 h_2 \tag{27}$$

This vector will be pointing in the outward direction with respect to the domain if directions $(\boldsymbol{s}, \boldsymbol{m})$ of the considered element are such that their cross product is outward oriented (this is only a matter of definition of the element nodes numbering).

The Jacobian matrix is defined as

$$\mathbf{J}^k = \left\{\frac{\partial \boldsymbol{x}}{\partial \xi}, \frac{\partial \boldsymbol{x}}{\partial \eta}, \boldsymbol{n}\right\}^T$$

and the determinant of the Jacobian matrix to be used in boundary integrals of Equation (5) for the kth element, by definition of an elementary surface element and with Equations (25) and (27), is given by

$$|\mathbf{J}^k(\xi, \eta)| = h_1 h_2 \quad \text{for } k = 1, \ldots, M_\Gamma \quad \text{on } \Gamma \tag{28}$$

which can be analytically calculated at any point of the element Γ_e^k, by using Equations (23)–(25), with Equation (21).

After transformation, the following discretized forms are obtained for the integrals in Equation (5):

$$\int_{\Gamma(\boldsymbol{x})} \frac{\partial \phi}{\partial n} G_l \, \mathrm{d}\Gamma = \sum_{j=1}^{N_\Gamma} \left\{ \sum_{k=1}^{M_\Gamma} \int_{\Gamma_{\xi,\eta}} N_j(\xi,\eta) G(\boldsymbol{x}(\xi,\eta), \boldsymbol{x}_l) \left|\mathbf{J}^k(\xi,\eta)\right| \mathrm{d}\xi \, \mathrm{d}\eta \right\} \frac{\partial \phi}{\partial n}(\boldsymbol{x}_j)$$
$$= \sum_{j=1}^{N_\Gamma} \left\{ \sum_{k=1}^{M_\Gamma} D_{lj}^k \right\} \frac{\partial \phi_j}{\partial n} = \sum_{j=1}^{N_\Gamma} K_{lj}^d \frac{\partial \phi_j}{\partial n} \tag{29}$$

$$\int_{\Gamma(\boldsymbol{x})} \phi \frac{\partial G_l}{\partial n} \, \mathrm{d}\Gamma = \sum_{j=1}^{N_\Gamma} \left\{ \sum_{k=1}^{M_\Gamma} \int_{\Gamma_{\xi,\eta}} N_j(\xi,\eta) \frac{\partial G(\boldsymbol{x}(\xi,\eta), \boldsymbol{x}_l)}{\partial n} \left| \mathbf{J}^k(\xi,\eta)\right| \mathrm{d}\xi \, \mathrm{d}\eta \right\} \phi(\boldsymbol{x}_j)$$
$$= \sum_{j=1}^{N_\Gamma} \left\{ \sum_{k=1}^{M_\Gamma} E_{lj}^k \right\} \phi_j = \sum_{j=1}^{N_\Gamma} K_{lj}^n \phi_j \tag{30}$$

in which $l = 1, \ldots, N_\Gamma$ and $\mathbf{D}^k$ and $\mathbf{K}^d$ denote so-called local (i.e., for element k) and global (i.e., assembled) Dirichlet matrices, and $\mathbf{E}^k$ and $\mathbf{K}^n$ are Neumann matrices. Note j is now expressed in the global node numbering on the boundary and denotes nodal values for element k. Expressions for the Green's function, the shape functions, and the Jacobian to be used in Equations (29) and (30) are given by Equations (3), (19), (21), and (28) respectively.

Using Equations (29) and (30), the discretized form of the BIE (5) finally reads

$$\alpha_l u_l = \sum_{j=1}^{N_\Gamma} \{K_{lj}^d \, q_j - K_{lj}^n \, u_j\} \tag{31}$$

in which $l = 1, \ldots, N_\Gamma$.

Boundary conditions are introduced in Equation (31); these are: (i) Dirichlet conditions for $u = \phi$ or $\partial\phi/\partial t$ (Equations (12) or (13)); and (ii) Neumann conditions for $q = \partial\phi/\partial n$ or $\partial^2\phi/\partial t \, \partial n$ (e.g., Equations (9), (10) or (14), (15)). The final algebraic system is assembled by moving nodal unknowns to the left-hand side and keeping specified terms on the right-hand side

$$\{C_{pl} + K_{pl}^n\} u_p - K_{gl}^d \, q_g = K_{pl}^d \overline{q_p} - \{C_{gl} + K_{gl}^n\} \overline{u_g} \tag{32}$$

where $l = 1, \ldots, N_\Gamma$; $g = 1, \ldots, N_g$ refers to nodes with Dirichlet condition on boundary Γ_f and $p = 1, \ldots, N_p$ refers to nodes with Neumann condition on boundary $\Gamma_{r1} \cup \Gamma_{r2} \cup \Gamma_b$. C is a diagonal matrix made of coefficients α_l.

2.3.4. Solution of the algebraic system of equations. The solution of the algebraic system of equations (32) initially implemented in the 3D-NWT was based on Kaletsky's direct lower–upper (LU) elimination method, for which the CPU time is proportional to the cube of the number of nodes in the discretization. This method was used in some of the applications presented hereafter, which have small or moderate grid sizes, and were run on a Mac G3-266 MHz powerbook or a G4-450 MHz computer. As we will see, for such small cases, the assembling of the system matrix through numerical integration, which is proportional to the number of elements (i.e., nodes), is more time consuming than the solution of the system itself.

The last applications presented in this paper, however, have much larger grid sizes and were run on a CRAY-C90 supercomputer. For such cases, the solution of the system matrix takes an increasingly large part of the total CPU time, and it is desirable to use a (faster) iterative

method to solve Equations (32). The 'generalized minimal residual' (GMRES) algorithm, also used by Xü and Yue [35,36], was implemented in the 3D-NWT, with preconditioning by the 'symmetric successive overrelaxation' (SSOR) method (relaxation parameter equal to 0.6), with an initial solution equal to that of the earlier time step. The downside, however, is that for the type of time stepping scheme used here, two full systems of equations must be solved at each time step—one for ϕ and one for $\partial\phi/\partial t$—with an iterative method, whereas with a direct method the solution of the second system takes only a few per cent of the time needed to solve the first system. Nevertheless, results showed that for large systems of say more than 2000 nodes and a similar accuracy, the GMRES-SSOR method is faster when used in the 3D-NWT than the direct solution.

2.3.5. Rigid mode method. Coefficients C_{ll} in Equation (32) can be obtained through a direct, purely geometric, calculation of solid angles θ_l at nodes of the discretized boundary. These coefficients, however, can be indirectly obtained through a more accurate and efficient approach, referred to as 'rigid mode' method by analogy with structural analysis problems (Brebbia [12]).

By considering a homogeneous Dirichlet problem, where a uniform field $\bar{u} = cst \neq 0$ is specified over the whole boundary Γ (thus $N_\Gamma = N_g$), one can show that normal gradients q must vanish at each node. Thus, Equation (32) simplifies to

$$\{C_{jl} + K^n_{jl}\}\overline{u_j} = 0 \tag{33}$$

which requires that the summation in curly brackets vanishes for all l. Thus, by isolating the diagonal terms in the left-hand side, we get

$$\{C_{ll} + K^n_{ll}\} = -\sum_{j(\neq l)=1}^{N_\Gamma} K^n_{jl}, \quad l = 1, \ldots, N_\Gamma \tag{34}$$

which specifies the value of the diagonal term of a row of Equation (33) as minus the sum of its off-diagonal coefficients. These diagonal terms are directly substituted in the discretized system (32).

This method was shown to significantly improve the conditioning of algebraic systems such as Equation (32), and thus the accuracy of their numerical solution [18] (particularly for iterative methods). Physically, for potential flows this also corresponds to specifying that the discretized problem exactly satisfies a zero global flux condition in a specific case.

2.3.6. Discretized boundary conditions at corners. Boundary conditions and normal directions are in general different on intersecting parts of the boundary, such as between the free surface or the bottom, and the lateral boundary of the computational domain (Figure 1). Such intersections are referred to as edges, and corresponding discretization nodes as corners. To be able to specify such differences in the model corners are represented by double-nodes for which co-ordinates are identical but normal vectors are different [18,46]. Thus, two different discretized BIEs (Equation (32)) are expressed for each node of a corner double-node.

For Dirichlet–Neumann boundary conditions we have, for instance, equations (i) for $l = p$ on the wavemaker boundary Γ_{r1}; and (ii) for $l = f$ on the free surface Γ_f. Since the potential

must be unique at a given location, however, one of these two BIEs must be modified in the final discretized system, to explicitly satisfy $\phi_p = \overline{\phi}_f$ (i.e., 'continuity of the potential'), where the overline indicates that the potential is specified on the free surface. For Neumann–Neumann boundary conditions at corners we have, for instance, equations (i) for $l = p$ on the wavemaker boundary Γ_{r1}; and (ii) for $l = b$ on the bottom Γ_b. The potential continuity equation for this case reads $\phi_p - \phi_b = 0$, both of these being unknown. Similar continuity relationships are expressed for $\partial\phi/\partial t$ at corners, in the corresponding BIE.

Note at the intersection between three boundaries, triple-nodes are specified for which three BIE equations are expressed, two of which are replaced in the final algebraic system by equations specifying continuity of the potential (and of $\partial\phi/\partial t$).

2.3.7. Grid generation. A simple and efficient method is implemented in the model for generating discretizations in the 3D-NWT with a minimum number of parameters. Referring to Figure 1, the grid for a typical problem is generated by specifying the geometrical parameters: x_0, d_0, depth h_0, the length l_0 in the x-direction and width w_0 in the y-direction, and the varying depth $b(x, y)$; the latter being also automatically calculated for a simple sloping bottom or a ridge. Discretization parameters M_x, M_y, and M_z are also given, which represent the number of MII quadrilateral elements in each direction. Note because of the way tangential derivatives are calculated (see below), there must be at least four elements in each direction.

2.4. Numerical integrations

Due to their complex analytical form, integrals in Equations (29) and (30) are numerically calculated for each collocation point $\boldsymbol{x}_l$. For each element k these integrals are represented by local matrices D_{lj}^k and E_{lj}^k.

When the collocation node l does not belong to the integrated quadrilateral element (i.e., $l \neq j(k) = 1, \ldots, 4$), a standard Gauss–Legendre quadrature method is used. When node l does belong to the element (i.e., Figure 3, $j = l$) distance r in Green's function and its normal gradient becomes zero at one of the nodes of the element (Equations (3) and (4)). It can be shown [12] that when $j = l$, integrals D_{lj}^k are weakly singular (thus integrable with finite L^2-norm), whereas integrals E_{lj}^k are non-singular. For the former integrals, special methods of 'singularity extraction' are detailed below. For the latter integrals, in fact, the strong singularity occurring when $r \to 0$ was already removed, to become part of coefficients α_l, and it can be shown that the remaining part is proportional to the boundary curvature at $\boldsymbol{x}_l$. In any case, when the 'rigid mode method' is used, terms such as E_{ll}^k are indirectly calculated in their global form K_{ll}^n by Equation (34).

Finally, due to the form of Green's function (3), non-singular integrals may still have a highly varying kernel when distance r becomes small, albeit non-zero, in the neighborhood of a collocation point. Such situations may occur near intersections of boundary parts (e.g., such as between the free surface and lateral boundaries) or in other regions of the free surface, such as overturning breaker jets, where nodes are close to elements on different parts of the boundary. In such cases, a standard Gauss quadrature, with a fixed number of integration points, may fail to accurately calculate such integrals. One thus talks of 'almost' or 'quasi-singular' integrals. Grilli and Subramanya [47], for instance, showed for two-dimensional

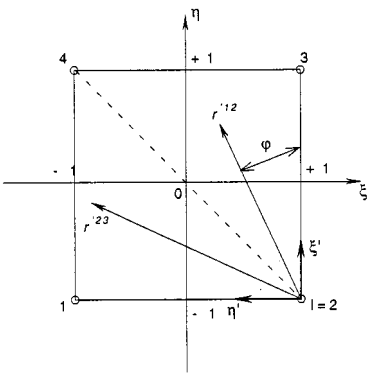

Figure 3. Sketch of co-ordinate transformations for weakly singular integrals in a quadrilateral element $\Gamma_{\xi,\eta}$, part of the 16-node cubic MII reference element (Figure 2). Axes (ξ', η') can be located at points $l = 1, \ldots, 4$. The case of collocation node $l = 2$ is given as an example.

problems that the loss of accuracy of Gauss integrations (with ten integration points) for such quasi-singular integrals may be several orders of magnitudes, when the distance to the collocation node becomes very small. For such two-dimensional cases, Grilli and Svendsen [46] developed an adaptive integration scheme based on a binary subdivision of the reference element and obtained almost arbitrary accuracy for the quasi-singular integrals when increasing the number of subdivisions. This method, however, can be computationally expensive and Grilli and Subramanya [47] developed a more efficient method that essentially redistributes integration points around the location of the quasi-singularity (point of minimum distance from an element k to the nearest collocation node $\boldsymbol{x}_l$). A method similar to Grilli and Svendsen's but applicable to three-dimensional problems is implemented in this study, and detailed below.

2.4.1. Regular integrals. For 3D-MII elements, regular integrals in Equations (29) and (30) are calculated with a bi-directional Gauss–Legendre quadrature method, with N_Λ points in each direction. These integrals take the form

$$I_{lj}^k = \int_{-1}^{+1} \int_{-1}^{+1} \mathscr{F}_{lj}^k(\xi, \eta)\, \mathrm{d}\xi\, \mathrm{d}\eta = \sum_{g=1}^{N_\Lambda} \sum_{h=1}^{N_\Lambda} w_g w_h \mathscr{F}_{lj}^k(\lambda_g, \lambda_h) \tag{35}$$

where $\mathscr{F}_{lj}^k$ represents either one of the kernels in integrals D_{lj}^k or E_{lj}^k, and (w_i, w_j) and (λ_g, λ_h) are Gauss weights and points respectively.

For more efficiency in the numerical model, once N_Λ is selected values of one-dimensional shape functions $N_c'(\mu(\chi, \chi_0))$ and their derivatives with respect to μ are precalculated for $\chi = \lambda_i$ $(i = 1, \ldots, N_\Lambda)$, $c = 1, \ldots, 4$, and $\chi_0 = -1, -1/3$, and $1/3$. From these, the two-dimensional shape functions N_j and their partial derivatives are calculated with Equations (19) and (23).

2.4.2. Weakly singular integrals. Weakly singular integrals correspond to terms D_{lj}^k in Equation (29) for $j=l$. In this case, the singular kernel of the integrals is first modified in order to get a form to which a polar co-ordinate transformation removing the weak $1/r$ singularity can be applied. This is followed by further changes of variable and a final Gauss–Legendre numerical quadrature (Badmus *et al.* [48]). We have

$$D_{lj}^k = \int_{\Gamma_{\xi,\eta}} f_j^k(\xi,\eta) G(\boldsymbol{x}(\xi,\eta), \boldsymbol{x}_l)\,\mathrm{d}\xi\,\mathrm{d}\eta \quad \text{with } f_j^k(\xi,\eta) = N_j(\xi,\eta)\left|\mathbf{J}^k(\xi,\eta)\right| \tag{36}$$

that is

$$D_{lj}^k = \frac{1}{4\pi}\int_{-1}^{+1}\int_{-1}^{+1} \frac{1}{r(\boldsymbol{x}(\xi,\eta),\boldsymbol{x}_l)} f_j^k(\xi,\eta)\,\mathrm{d}\xi\,\mathrm{d}\eta \tag{37}$$

where the singularity is located at node $\boldsymbol{x}_l$ of the discretization, corresponding to co-ordinates (ξ_l, η_l) on the reference element.

A new co-ordinate system, centered on node (ξ_l, η_l), is defined within the reference element as

$$\xi' = \xi - \xi_l \quad \text{and} \quad \eta' = \eta - \eta_l \tag{38}$$

and Equation (37) becomes

$$D_{lj}^k = \frac{1}{4\pi}\iint \frac{1}{r'} F_j^k(\xi',\eta')\,\mathrm{d}\xi'\,\mathrm{d}\eta' \tag{39}$$

with

$$r' = \sqrt{\xi'^2 + \eta'^2} \quad \text{and} \quad F_j^k(\xi',\eta') = \frac{r'}{r(\boldsymbol{x}(\xi(\xi'),\eta(\eta')),\boldsymbol{x}_l)} f_j^k(\xi(\xi'),\eta(\eta')) \tag{40}$$

where the function F_j^k is non-singular (as could be seen by taking its limit for $r\to 0$) and the integration limits for ξ' and η' depend on the position of the singularity.

Polar co-ordinates (r', φ) centered on (ξ_l, η_l) are then introduced (Figure 3) such that

$$\xi' = r'\cos\left\{\varphi + (l-1)\frac{\pi}{2}\right\} \quad \text{and} \quad \eta' = r'\sin\left\{\varphi + (l-1)\frac{\pi}{2}\right\} \tag{41}$$

with $l=1,\ldots,4$. Noting that $\mathrm{d}\xi'\,\mathrm{d}\eta' = r'\,\mathrm{d}r'\,\mathrm{d}\varphi$ and accounting for the geometry of the reference element, Equation (39) becomes

$$D_{lj}^k = \frac{1}{4\pi}\left\{\int_0^{\pi/4}\mathrm{d}\varphi\int_0^{2/\cos\varphi} F_j^k(r',\varphi)\,\mathrm{d}r' + \int_{\pi/4}^{\pi/2}\mathrm{d}\varphi\int_0^{2/\sin\varphi} F_j^k(r',\varphi)\,\mathrm{d}r'\right\} \tag{42}$$

where Equations (38) and (41) are used to relate (r', φ) to (ξ, η) in F_j^k. Limits of integrations in Equation (42) are transformed into $[-1, +1]$ by a last change of variable to (r'', φ') and we get

$$D_{lj}^k = \frac{1}{64} \int_{-1}^{+1} \mathrm{d}\varphi' \left\{ r_m'^{12} \int_{-1}^{+1} F_j^k(r'^{12}, \varphi^{12})\, \mathrm{d}r'' + r_m'^{23} \int_{-1}^{+1} F_j^k(r'^{23}, \varphi^{23})\, \mathrm{d}r'' \right\} \tag{43}$$

which can be integrated by a bi-directional Gauss–Legendre quadrature method as

$$D_{lj}^k = \frac{1}{64} \sum_{i=1}^{N_\Lambda} \sum_{j=1}^{N_\Lambda} w_i w_j \{ r_m'^{12} F_j^k(r'^{12}, \varphi^{12}) + r_m'^{23} F_j^k(r'^{23}, \varphi^{23}) \} \tag{44}$$

where (w_i, w_j) are Gauss weights, with

$$\varphi^{12} = \frac{\pi}{8}(1 + \lambda_i) \quad \text{and} \quad \varphi^{23} = \frac{\pi}{8}(3 + \lambda_i) \tag{45}$$

$$r_m'^{12} = \frac{2}{\cos \varphi^{12}} \quad \text{and} \quad r_m'^{23} = \frac{2}{\sin \varphi^{12}} \tag{46}$$

and

$$r'^{12} = \frac{r_m'^{12}}{2}(1 + \lambda_j) \quad \text{and} \quad r'^{23} = \frac{r_m'^{23}}{2}(1 + \lambda_j) \tag{47}$$

where $(\lambda_i, \lambda_j) \in [-1, +1]$ are Gauss points.

Again, for more efficiency, once N_Λ is selected in the numerical model, values of φ^{12}, φ^{23}, $r_m'^{12}$, $r_m'^{23}$, r'^{12}, and r'^{23} are precalculated for (λ_i, λ_j) values, from which $(\xi_{ij}^{12,23}, \eta_{ij}^{12,23})$ values are obtained using Equations (38) and (41) for $l = 1, \ldots, 4$. Then, one-dimensional shape functions $N_c'(\mu(\chi, \chi_0))$ and their derivatives with respect to μ, to be used in Equations (19) and (23), are precalculated for $\chi = \xi_{ij}^{12,23}$ or $\eta_{ij}^{12,23}$ $(i, j = 1, \ldots, N_\Lambda)$; $c, l = 1, \ldots, 4$; and $\chi_0 = -1, -1/3,$ and $1/3$. From these, the two-dimensional shape functions N_j and their partial derivatives are calculated using Equations (19) and (23).

2.4.3. Quasi-singular integrals. To identify possible quasi-singular integrals in the discretized domain, both distance and intercept angle thresholds are checked for each collocation node $l = 1, \ldots, N_\Gamma$ and each quadrilateral boundary element $k = 1, \ldots, M_\Gamma$.

For each element k, the minimum intercept angle $\beta_{\min}$ and the maximum number of binary subdivisions $S_{\max}$ are specified as input. An equivalent diameter is calculated as

$$D^k = \frac{1}{2} \mathrm{MAX}(d_{13}, d_{24}) \tag{48}$$

where d_{ab} indicates distance from node a to b in k. Two planes are defined based on triplets of element nodes as $(\boldsymbol{r}_{12}, \boldsymbol{r}_{13})$ and $(\boldsymbol{r}_{12}, \boldsymbol{r}_{14})$, where $\boldsymbol{r}_{ab} = \boldsymbol{x}_b - \boldsymbol{x}_a$. Normal unit vectors to these planes are

$$\boldsymbol{n}_{23} = \frac{\boldsymbol{r}_{12} \times \boldsymbol{r}_{13}}{|\boldsymbol{r}_{12} \times \boldsymbol{r}_{13}|} \quad \text{and} \quad \boldsymbol{n}_{24} = \frac{\boldsymbol{r}_{12} \times \boldsymbol{r}_{14}}{|\boldsymbol{r}_{12} \times \boldsymbol{r}_{14}|} \tag{49}$$

The following distance parameters are calculated for each collocation node $l = 1, \ldots, N_\Gamma$

$$\delta_1 = \frac{D^k}{d_{lc}}, \qquad \delta_2 = \frac{D^k}{\mathrm{MIN}(d_{lj})}, \quad \text{and} \quad \delta_3 = \frac{D^k}{\mathrm{MIN}(d_{l23}, d_{l24})} \tag{50}$$

for $j = 1, \ldots, 4$ element nodes $\boldsymbol{x}_j^k$, where $\boldsymbol{x}_c^k = \overline{\boldsymbol{x}_j^k}$ denotes co-ordinates of the element geometric center and $d_{lab} = \boldsymbol{r}_{l1} \cdot \boldsymbol{n}_{ab}$ is the minimum distance from point l to the plane ab. The intercept angle for node l and element k is calculated as $\beta = 2 \arctan \delta_\beta$, with

$$\delta_\beta = \frac{\delta_1^2}{\delta_3} \quad \text{for } d_{lc} > D^k \frac{\delta_1 \delta_3}{\sqrt{\delta_1^2 + \delta_3^2}}$$

$$\delta_\beta = \delta_3 \quad \text{for } d_{lc} \le D^k \frac{\delta_1 \delta_3}{\sqrt{\delta_1^2 + \delta_3^2}} \quad \text{and} \quad \mathrm{MIN}(d_{l23}, d_{l24}) \neq 0 \tag{51}$$

In the latter case, $\delta_\beta = \beta = 0$ otherwise, which corresponds to point l lying within the plane of a plane element.

Following the 'adaptive integration' method introduced by Grilli and Svendsen [46] for two-dimensional problems, quasi-singular integrals for element k are performed by dividing the reference element into $N_s = 2^S$ segments of length $\Delta S = 2/N_s$ in both the ξ- and η-direction, where $S \le S_{\max}$ denotes the number of binary subdivisions. This number is selected as follows for node l, as a function of values of β and parameters in Equations (50):

$$S = \mathrm{INT}\left\{(\log 2) \log\left\{\frac{\delta_S}{\tan \beta_{\min}}\right\} + 0.4999\right\} \quad \text{for } \beta > \beta_{\min} \quad \text{and} \quad \delta_1 > 1 \tag{52}$$

with

$$\delta_S = (\delta_3, \delta_1) \quad \text{for } \mathrm{MIN}(d_{l23}, d_{l24}) \quad (>, =0)$$

Otherwise $\delta_S = \delta_2$ and the same equation applies for calculating S.

After subdivision, variations of intrinsic co-ordinates over each sub-element are transformed back to $[-1, +1]$ intervals. We thus have for quasi-singular integrals such as in Equation (35)

$$\int_{-1}^{+1} \int_{-1}^{+1} \mathscr{F}_{lj}^k(\xi, \eta)\, \mathrm{d}\xi\, \mathrm{d}\eta = \sum_{v=1}^{N_s} \sum_{w=1}^{N_s} \int_{-1}^{+1} \int_{-1}^{+1} \mathscr{F}_{lj}^k(\xi(\xi'_v), \eta(\eta'_w))\, \mathrm{d}\xi'\, \mathrm{d}\eta' \tag{53}$$

with

$$\xi = \frac{\xi'_v}{N_s} + \frac{\xi_r + \xi_\ell}{2}, \qquad \eta = \frac{\eta'_w}{N_s} + \frac{\eta_r + \eta_\ell}{2} \tag{54}$$

and $\xi_\ell = 2(v-1)/N_s - 1$, $\eta_\ell = 2(w-1)/N_s - 1$, $\xi_r = \xi_\ell + \Delta S$, and $\eta_r = \eta_\ell + \Delta S$. Integrals for each (v, w) combination in Equation (53) are calculated with the Gauss–Legendre quadrature method, as in Equation (35).

2.5. Higher-order tangential derivatives

Higher-order derivatives, with respect to tangential directions $\boldsymbol{s}$ and $\boldsymbol{m}$, of the geometry and field variables are needed for the expression of coefficients in Taylor series expansions (11) and (12), used for the time updating of free surface nodes. Tangential derivatives are also needed on wavemaker boundary nodes for the expression of boundary conditions such as Equation (14).

As discussed above, a BEM discretization is defined within each 3D-MII boundary element to calculate boundary integrals, by way of a curvilinear change of variables to the reference element $\Gamma_{\xi,\eta}$. For the calculation of higher-order tangential derivatives at discretization nodes, a specific local fourth-order interpolation is defined, in a way similar to the sliding polynomial used by Grilli *et al.* [18] in their two-dimensional model. In the three-dimensional model, a bi-quartic local interpolation, based on the product of two one-dimensional, fourth-order, 5-node shape functions, $S'_c(\mu)$ $(\mu \in [-1, +1];\ c = 1, \ldots, 5)$, is defined over a 5×5 node local/sliding grid to calculate derivatives at one node of the grid (usually the central node; Figure 4). Variations of the geometry and field variables are thus locally defined by

$$\boldsymbol{x}(\xi, \eta) = S_j(\xi, \eta)\boldsymbol{x}_j \tag{55}$$

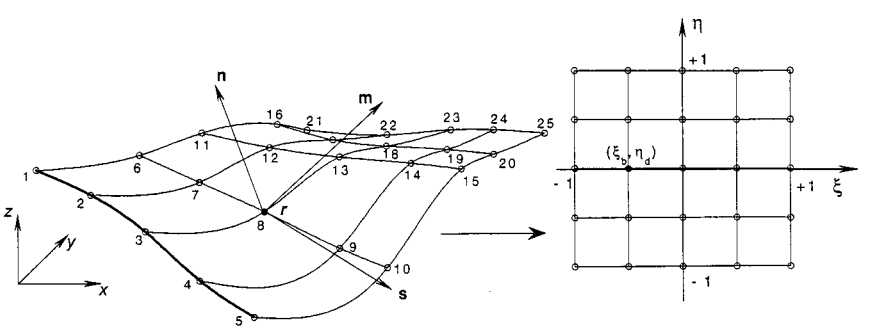

Figure 4. Sketch of local interpolation by fourth-order two-dimensional sliding polynomials of (ξ, η), for calculating tangential derivatives in curvilinear axes $(\boldsymbol{s}, \boldsymbol{m}, \boldsymbol{n})$ at point $\boldsymbol{r}$ of the boundary. The case with a boundary edge located to the left of the considered area and $j = 8$ is plotted as an example, for which $\xi_b = -1/3$ and $\eta_d = 0$.

$$v(\xi, \eta) = S_j(\xi, \eta) v_j \tag{56}$$

where $j = 1, \ldots, 25$; v denotes ϕ, $\partial\phi/\partial n$, or $\partial\phi/\partial t$, and the two-dimensional shape functions are defined by

$$S_j(\xi, \eta) = S'_b(\xi) S'_d(\eta) \tag{57}$$

with b and $d = 1, \ldots, 5$; $j = 5(d-1) + b$. For more efficiency in the model, values of shape functions S_j and their first and second partial derivatives with respect to ξ and η (calculated by differentiation of Equation (57)) are precalculated for $j = 1, \ldots, 25$, at all points (ξ_b, η_d) of the local grid (for b, $d = 1, \ldots, 5$).

As in the BEM discretization, a local curvilinear co-ordinate system is defined at each boundary node $(\boldsymbol{s}, \boldsymbol{m}, \boldsymbol{n})$ by equations similar to Equations (23)–(27). Derivatives of ϕ and $\partial\phi/\partial t$ with respect to normal direction $\boldsymbol{n}$ are obtained by solving the BIE (5) for ϕ and $\partial\phi/\partial t$. Derivatives of the geometry and field variables with respect to tangential directions $\boldsymbol{s}$ and $\boldsymbol{m}$ are computed at boundary nodes, by differentiating Equations (55) and (56) and taking the value for $\xi = \eta = 0$, in general, or any other location in the grid ($\xi_b = (2b-6)/4$, $\eta_d = (2d-6)/4$), for nodes located close to boundary edges. We define the following notations:

$$(\ )_s \equiv \frac{\partial}{\partial s} = \frac{1}{h_1}\frac{\partial}{\partial \xi}, \qquad (\ )_m \equiv \frac{\partial}{\partial m} = \frac{1}{h_2}\frac{\partial}{\partial \eta}, \quad \text{and} \quad (\ )_n \equiv \frac{\partial}{\partial n} \tag{58}$$

and

$$(\ )_{ss} \equiv \frac{1}{h_1^2}\frac{\partial^2}{\partial \xi^2}, \qquad (\ )_{sm} \equiv \frac{1}{h_1 h_2}\frac{\partial^2}{\partial \xi\, \partial \eta}, \quad \text{and} \quad (\ )_{mm} \equiv \frac{1}{h_2^2}\frac{\partial^2}{\partial \eta^2} \tag{59}$$

Based on Equation (1) and with notations (58), the particle velocity is expressed in the local co-ordinate system on the boundary by

$$\boldsymbol{u} = \nabla\phi = \phi_s \boldsymbol{s} + \phi_m \boldsymbol{m} + \phi_n \boldsymbol{n} \tag{60}$$

where ϕ_s and ϕ_m denote tangential velocities in the $\boldsymbol{s} = \boldsymbol{x}_s$ and $\boldsymbol{m} = \boldsymbol{x}_m$ directions respectively (Equations (24) and (58)), and $\boldsymbol{n} = \boldsymbol{s} \times \boldsymbol{m}$. Laplace's equation (2) is similarly expressed and, after some transformations, leads to

$$\frac{\partial^2\phi}{\partial n^2} = -\phi_{ss} - \phi_{mm} + \phi_s\{\boldsymbol{x}_{ss}\cdot\boldsymbol{s} - \boldsymbol{x}_{sm}\cdot\boldsymbol{m}\} + \phi_m\{\boldsymbol{x}_{mm}\cdot\boldsymbol{m} - \boldsymbol{x}_{sm}\cdot\boldsymbol{s}\} + \phi_n\{\boldsymbol{x}_{ss}\cdot\boldsymbol{n} + \boldsymbol{x}_{mm}\cdot\boldsymbol{n}\} \tag{61}$$

Note the last term in curly brackets represents the sum of curvatures in two orthogonal directions. By applying the material derivative to Equation (60), after some calculations the particle acceleration is similarly expressed in the local co-ordinate system on the boundary by (where all indices represent partial derivatives)

$$\frac{\mathrm{D}\boldsymbol{u}}{\mathrm{D}t} = \boldsymbol{s}\{\phi_{ts} + \phi_s\phi_{ss} + \phi_m\phi_{sm} + \phi_n\phi_{ns} - \phi_s^2\{\boldsymbol{x}_{ss}\cdot\boldsymbol{s}\} + \phi_m^2\{\boldsymbol{x}_{mm}\cdot\boldsymbol{s}\} - \phi_n\phi_m\{\boldsymbol{x}_{sm}\cdot\boldsymbol{n}\}\}$$
$$+ \boldsymbol{m}\{\phi_{tm} + \phi_s\phi_{sm} + \phi_m\phi_{mm} + \phi_n\phi_{nm} + \phi_s^2\{\boldsymbol{x}_{ss}\cdot\boldsymbol{m}\} - \phi_m^2\{\boldsymbol{x}_{mm}\cdot\boldsymbol{m}\} - \phi_n\phi_s\{\boldsymbol{x}_{sm}\cdot\boldsymbol{n}\}\}$$
$$+ \boldsymbol{n}\{\phi_{tn} + \phi_s\phi_{ns} + \phi_m\phi_{nm} - \phi_n\{\phi_{ss} + \phi_{mm}\} + \phi_s^2\{\boldsymbol{x}_{ss}\cdot\boldsymbol{n}\} + \phi_m^2\{\boldsymbol{x}_{mm}\cdot\boldsymbol{n}\}$$
$$+ 2\phi_s\phi_m\{\boldsymbol{x}_{sm}\cdot\boldsymbol{n}\} + \phi_n^2\{\boldsymbol{x}_{ss}\cdot\boldsymbol{n} + \boldsymbol{x}_{mm}\cdot\boldsymbol{n}\} + \phi_n\phi_s\{\boldsymbol{x}_{ss}\cdot\boldsymbol{s} - \boldsymbol{x}_{sm}\cdot\boldsymbol{m}\}$$
$$+ \phi_n\phi_m\{\boldsymbol{x}_{mm}\cdot\boldsymbol{m} - \boldsymbol{x}_{sm}\cdot\boldsymbol{s}\}\} \tag{62}$$

With Equation (6), the second-order term in the Taylor series expansion (11) is given by Equation (62), whereas with Equation (7), the second-order term in Equation (12) is given by

$$\frac{\mathrm{D}^2\phi}{\mathrm{D}t^2} = -gw + \boldsymbol{u}\cdot\frac{\mathrm{D}\boldsymbol{u}}{\mathrm{D}t} - \frac{1}{\rho}\frac{\mathrm{D}p_\mathrm{a}}{\mathrm{D}t} \tag{63}$$

where Equations (60) and (62) are used to calculate the second term on the right-hand side, and w denotes the vertical particle velocity.

Finally, for a wavemaker boundary using Equations (8) and (60), Equation (14) becomes

$$\overline{\frac{\partial^2\phi}{\partial t\,\partial n}} = \frac{\mathrm{d}(\boldsymbol{u}_p\cdot\boldsymbol{n})}{\mathrm{d}t} - \phi_s\phi_{ns} - \phi_m\phi_{nm} - \phi_n\phi_{nn} \quad \text{on } \Gamma_{r1}(t) \tag{64}$$

Laplace's equation in the form of Equation (61) can be used to express the last term in Equation (64). For a plane solid wavemaker paddle, for instance, we get

$$\overline{\frac{\partial^2\phi}{\partial t\,\partial n}} = (\dot{\boldsymbol{u}}_p\cdot\boldsymbol{n}) + \left(\boldsymbol{u}_p\cdot\frac{\mathrm{d}\boldsymbol{n}}{\mathrm{d}t}\right) + (\boldsymbol{u}_p\cdot\boldsymbol{n})\{\phi_{ss} + \phi_{mm}\} - \phi_s\phi_{ns} - \phi_m\phi_{nm} \tag{65}$$

on $\Gamma_{r1}(t)$, where $\dot{\boldsymbol{u}}_p = \mathrm{d}u_p/\mathrm{d}t$ denotes the absolute wavemaker acceleration and $\mathrm{d}\boldsymbol{n}/\mathrm{d}t = \boldsymbol{\omega}\times\boldsymbol{n}$, for a plane wavemaker rotating with angular velocity $\boldsymbol{\omega}$.

2.6. Free surface node regridding

In the study of overturning waves, it is desirable to have a means of refining the mesh discretization in areas of formation of breaker jets prior to their occurrence. In two-dimensional studies this was done by implementing a node regridding method in which a specified number of nodes were regridded at constant arc-length value in between two nodes selected on the free surface [22].

In the present three-dimensional case, a two-dimensional regridding method is implemented based on the same principle. However, here the method assumes a single-valued free surface $\eta(x, y)$ at the time of regridding, with a new mesh (x_i^n, y_i^n) (with $i = 1, \ldots, N_\mathrm{f}$; and N_f the number of nodes in the new mesh on the free surface) being defined with constant Δx and Δy intervals. The first step is to locate in which 3D-MII element k, in the old mesh free surface, each new node is located. Then we solve the following simultaneous polynomial equations for (ξ^n, η^n):

$$x_i^n - N_j(\xi^n, \eta^n)x_j^k = 0 \quad \text{and} \quad y_i^n - N_j(\xi^n, \eta^n)y_j^k = 0 \tag{66}$$

for $j = 1, \ldots, m$. This is done iteratively with a Newton–Raphson method. New free surface elevations z_i^n and field variables v_i^n are finally calculated (with $v = \phi$ or $\partial\phi/\partial n$) as

$$z_i^n = N_j(\xi^n, \eta^n)z_j^k \quad \text{and} \quad v_i^n = N_j(\xi^n, \eta^n)v_j^k \tag{67}$$

Computations are updated to the next time step based on the new fields, $\boldsymbol{x}$, ϕ, and $\partial\phi/\partial n$, regridded on the free surface.

2.7. Selection of mesh and time step size

Numerical errors in the model are a function of the size (i.e., distance between nodes) and degree (i.e., quadratic, cubic, ...) of the boundary elements used in the spatial discretization, both of which control the accuracy of the BEM solution of Laplace's equation (2), and of the size of the selected time step, Δt, which controls the accuracy of the time stepping method ($\mathcal{O}[(\Delta t)^3]$ in Equations (11) and (12)).

2.7.1. Adaptive time stepping. Thus, in each application, mesh and time step sizes must be properly selected in the model to ensure both an accurate numerical solution of governing equations and sufficient spatial and temporal resolution of the physical phenomena one wishes to analyze. Since for water waves such phenomena usually dynamically evolve as a function of the solution itself (e.g., breaker jets), mesh and time step sizes must be gradually adapted throughout computations.

In the present method, unless regridding is used mesh size is automatically adjusted in the MEL time updating. For instance, discretization nodes identical to fluid particles gather in regions of flow convergence. Thus, to adjust the time step, Grilli *et al.* [22,46] introduced an adaptive time stepping method in their two-dimensional model. By computing the propagation of fully non-linear solitary waves (Tanaka [49]) over constant depth in the model, for many spatio-temporal discretizations, they showed that an optimal mesh Courant number $\mathscr{C}_0$ exists for which numerical errors on mass and energy conservation reach a minimum (see next section). Therefore, at all times they adaptively selected the time step as

$$\Delta t = \mathscr{C}_0 \frac{\Delta|\boldsymbol{r}|^{\min}}{\sqrt{gh}} \tag{68}$$

where $\Delta|\boldsymbol{r}|^{\min}$ denotes the instantaneous minimum distance between nodes on the free surface, and h is a characteristic depth. For 2D-MII elements, Grilli and Subramanya [22] showed that $\mathscr{C}_0 \simeq 0.4$.

Since the present three-dimensional model uses similar numerical methods as in the two-dimensional model, the 'adaptive time stepping' method defined by Equation (68) is also used here. Tests of numerical accuracy as a function of mesh and time step size for 3D-MII elements are presented in the applications below for the propagation of a fully non-linear (i.e., numerically exact) solitary wave over constant depth.

2.7.2. Global assessment of numerical accuracy. At each time step, mass and energy conservation must be globally satisfied in the computational domain. Hence, measures of how well these are conserved provide a quantification of numerical accuracy as a function of spatial and temporal discretization parameters.

For $\rho = cst$, one can quantify errors on conservation of mass at all times by

$$\varepsilon_V(t) = \frac{V(t) - V_0}{V_0}, \quad \text{with } V(t) = \int_{\Omega(t)} \mathrm{d}\Omega = \int_{\Gamma(t)} z(\boldsymbol{e}_z \cdot \boldsymbol{n})\, \mathrm{d}\Gamma \tag{69}$$

where $\boldsymbol{e}_z$ denotes the vertical unit vector and V_0 the initial domain volume at $t = 0$. One can also check that the continuity equation (2) is accurately satisfied by calculating

$$\varepsilon_C(t) = \frac{\Delta t}{V_0} \int_{\Gamma(t)} \frac{\partial \phi}{\partial n}\, \mathrm{d}\Gamma \tag{70}$$

Kinetic energy in the computational domain is calculated as

$$e_K(t) = \frac{1}{2}\rho \int_{\Omega(t)} (\nabla\phi \cdot \nabla\phi)\, \mathrm{d}\Omega = \frac{1}{2}\rho \int_{\Gamma(t)} \phi \frac{\partial \phi}{\partial n}\, \mathrm{d}\Gamma \tag{71}$$

where an integration by part has been performed, and both the divergence theorem and Equation (2) have been used. Potential energy in the computational domain is calculated as

$$e_P(t) = \rho g \int_{\Omega(t)} z\, \mathrm{d}\Omega = \frac{1}{2}\rho g \int_{\Gamma(t)} z^2 (\boldsymbol{e}_z \cdot \boldsymbol{n})\, \mathrm{d}\Gamma \tag{72}$$

If there is no energy input, e.g., due to a wavemaker motion, total energy must be conserved in the computational domain. Errors on total energy conservation can thus be quantified at all times by

$$\varepsilon_E(t) = \left| \frac{E(t) - E_0}{E_0} \right| \quad \text{with } E(t) = e_K(t) + e_P(t) \tag{73}$$

where E_0 is the initial total energy in the domain.

Equations (69) and (72), however, include volume and potential energy for the whole domain. In some cases, such as for solitary waves, it is more useful to check these with respect to the free surface. Hence, based on these equations the error on conservation of volume with respect to $z = 0$ reads

$$\varepsilon_m(t) = \left| \frac{m(t) - m_0}{m_0} \right| \quad \text{with } m(t) = \int_{\Gamma_f(t)} z(\boldsymbol{e}_z \cdot \boldsymbol{n})\, \mathrm{d}\Gamma \tag{74}$$

where m_0 is the initial wave volume in the domain. Potential energy with respect to $z = 0$ reads

$$e_{P_0}(t) = \frac{1}{2}\rho g \int_{\Gamma_f(t)} z^2 (\boldsymbol{e}_z \cdot \boldsymbol{n})\, \mathrm{d}\Gamma \tag{75}$$

Hence, errors on total energy conservation for the wave motion can be quantified at all times by

$$\varepsilon_e(t) = \left| \frac{e(t) - e_0}{e_0} \right| \quad \text{with } e(t) = e_K(t) + e_{P_0}(t) \tag{76}$$

where e_0 is the initial total wave energy in the domain.

3. APPLICATIONS

3.1. Solitary wave propagation over constant depth: determination of optimal Courant number

As was done in the two-dimensional models by Grilli *et al.* [22,46], the optimal mesh Courant number $\mathscr{C}_0$ for the 3D-MII elements—corresponding to minimum numerical errors for a given discretization resolution—is found by computing the propagation of numerically exact solitary waves over constant depth h_0. Such solitary waves should keep permanent form, celerity, constant volume m above $z = 0$, and total energy e, while propagating in the model. Hence, numerical errors in the computations give a measure of discretization and time step effects on global numerical accuracy.

Figure 5 shows the sketch for the three-dimensional model set-up. The domain length is 15 times the depth h_0 and its width is set to $2h_0$. Two-dimensional solitary waves are obtained using the fully non-linear method by Tanaka [49]. These are made three-dimensional by specifying the two-dimensional profiles for each vertical cross-section of the three-dimensional discretization. Waves are initially defined by their shape η, potential ϕ and $\partial\phi/\partial n$ on the free surface, at time $t' = t\sqrt{g/h_0} = 0$ (see Reference [46] for details; note in the following dashes denote non-dimensional variables for which length is scaled by h_0 and time by $\sqrt{h_0/g}$). A strongly non-linear wave of height $H'_0 = 0.6$ is initially specified, with its crest located at

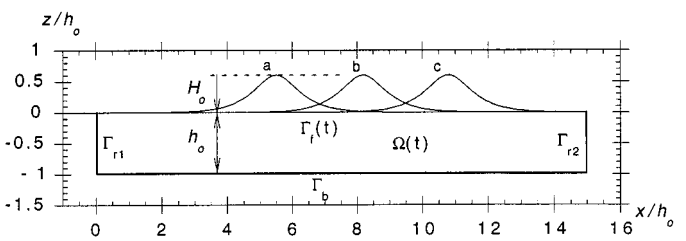

Figure 5. Sketch for the propagation of a 'Tanaka' solitary wave of initial height H_0 over constant depth h_0 in the 3D-NWT. Note only the vertical cross-section at $y = 0$ is shown in the figure, with (a) initial wave profile at $t'_0 = 0$, (b) intermediate wave profile, (c) final wave profile at $t'_f = 4$.

$x' = 5.5$, and propagated in various spatio-temporal discretizations. For this wave, Tanaka's method provides, $m'_0 = 3.87765$ and $e'_0 = 1.58547$.

Three different spatial discretizations are used in the computations, with initial distances between nodes $\Delta x'_0 = 0.25$, 0.33, and 0.50 respectively ($M_x = 60$, 45, and 30), and $\Delta y'_0 = 0.50$ ($M_y = 4$) on the free surface Γ_f and bottom Γ_b; $\Delta z'_0 = 0.25$ ($M_z = 4$) on the lateral boundaries Γ_{r1} and Γ_{r2}. Ten Gauss points are used per direction in the integrations ($N_\Lambda = 10$) and adaptive integration is specified in corner/edge elements. The Courant number is successively set to $\mathscr{C}_0 = 0.3$, 0.4, 0.5, and 0.6, thus defining 12 computational cases. This leads to initial time steps in between $\Delta t'_0 = 0.075$ and 0.30; the time step is then adapted in time based on Equation (68) as a function of the minimum instantaneous distance between nodes on the free surface. Computational errors on mass and energy conservation: $\varepsilon_m(t)$ and $\varepsilon_e(t)$ (Equations (74) and (76)) are calculated as a function of time for the propagation of the wave over four dimensionless time units, $t'_f = 4$, representing a varying number of time steps in each case. This also corresponds to a horizontal distance about five times the depth. Maximum relative errors on wave shape were also calculated for each case and found to follow the same trend while always being smaller or equal to errors on wave mass. Hence, these errors are not shown in detail here, but clearly indicate that the calculated wave shape converges well with grid size in this application. Finally note the initial wave used in the model is truncated at $x' = 0$, where the free surface elevation is $\eta' = 0.0057$. This results in slightly smaller initial wave volume and total energy than Tanaka's values; these reduced values are used in the calculation of relative numerical errors.

Computational errors are shown in Figure 6 for the 12 computed cases. Mean, r.m.s., and maximum error curves are given as a function of the spatial discretization resolution and Courant number. We first see that, in general, the smaller $\Delta x'_0$, the smaller the numerical errors. This indicates the convergence of results in the 3D-NWT with an increased resolution of the discretization (i.e., with N_Γ or M_Γ); more specifically, we see that there is more than one order of magnitude gain in accuracy when $\Delta x'_0$ is divided by two. Now, varying the mesh Courant number (i.e., the time step) for a given $\Delta x'_0$ we see that in many cases one or the other type of errors, ε_m or ε_e, decreases with $\mathscr{C}_0$. In each case, however, an optimal region with minimal errors is reached for either type of error around $\mathscr{C}_0 = 0.4$–0.5. For smaller $\mathscr{C}_0$, global errors probably re-increase due to the accumulation of round-off and truncation errors when using too many small time steps. Hence, for optimum accuracy and efficiency of computations, the Courant number should be specified to, say, $\mathscr{C}_0 \simeq 0.45$ in the model (this is close to the value obtained by Reference [22] for their 2D-NWT). Looking at error curves, however, it is clear that small variations around this value should not affect accuracy too much.

Finally, it should be mentioned that computational times were 630, 353, and 222 s of CPU per time step (on a Mac PowerBook G3-266MHz) for $\Delta x'_0 = 0.25$, 0.33, and 0.50 respectively, i.e., $N_\Gamma = 1270$, 970, and 670, or $M_\Gamma = 992$, 752, and 512. This indicates that, with respect to the coarser discretization (0.5), CPU time increases proportionally to roughly the power 1.3 and 1.6 of the ratio of numbers of nodes or elements for $\Delta x'_0 = 0.33$ and 0.25, respectively. The solution of the algebraic system in this implementation of the 3D-BEM model is direct and, hence, takes a CPU time proportional to the cube of the number of nodes in the discretization. Thus, the smaller exponent values obtained here indicate that the most time consuming part in

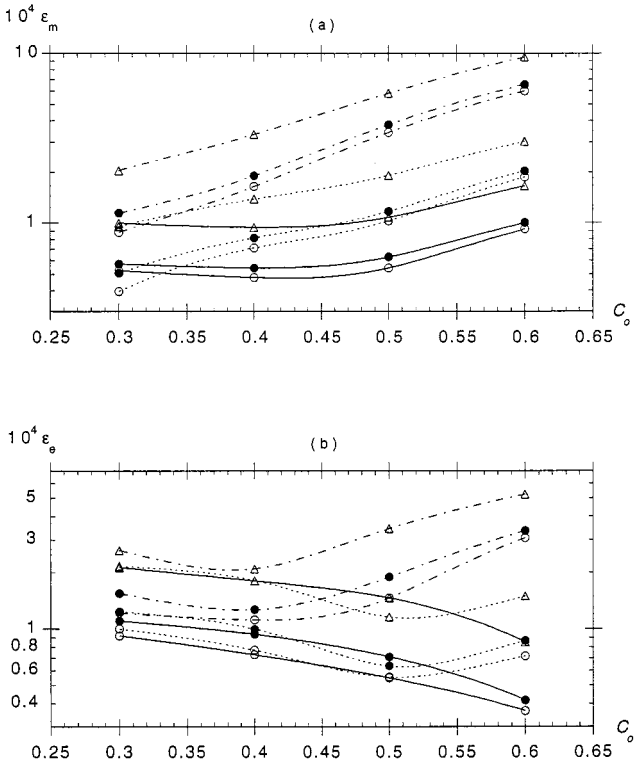

Figure 6. Relative numerical errors ($\times 10^4$) on: (a) volume conservation and (b) energy conservation. ○, Mean errors; ●, r.m.s. errors; and △, maximum errors for the propagation of an exact solitary wave of initial height $H'_0 = 0.6$ over constant depth, in the 3D-NWT (Figure 5): for $\Delta x'_0 = 0.25$ (—), 0.33 (- - -), and 0.50 (– – –), as a function of the Courant number, $\mathscr{C}_0$.

the computation is the assembling of the system matrix, through numerical integration, for which CPU time is proportional to the number of elements M_Γ (i.e., also roughly N_Γ). For much larger discretizations, however, it would be expected that the (direct) solution of the algebraic system take an increasingly larger part of the total CPU time (see last application).

3.2. Solitary wave shoaling over a plane slope: comparison with results in a 2D-NWT

Grilli *et al.* [5,6] calculated the shoaling and breaking of solitary waves over plane slopes in their 2D-FNPF-NWT and compared results with detailed laboratory experiments. They showed that computations of surface elevations matched experimental results within 2 per cent, up to the breaking point.

Similar computations are made here, in a narrow 3D-NWT of width $2h_0$, having no geometric variation in the transversal y-direction. A plane slope, $s = 1{:}15$, is specified in the

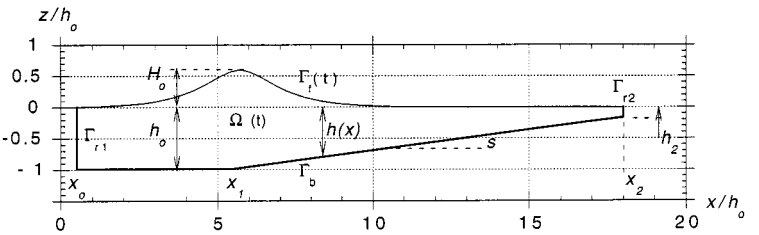

Figure 7. Sketch for the propagation of an exact solitary wave of initial height H_0 in depth h_0 over a plane slope s in the 3D-NWT. Note only the vertical cross-section at $y = 0$ is shown on the figure and, for convenience, the slope has been truncated at $x = x_2$, with $x_1 = x_0 + d_0$ and $x_2 = x_1 + (h_0 - h_2)/s$.

domain, starting at $x'_1 = d'_0 = 5.4$ and truncated at $x'_2 = 18$ with a depth of $h'_2 = 0.16$ (Figure 7). The initial wave is the same as the 'Tanaka' solitary wave used before, with $H'_0 = 0.6$ and its crest is initially located at $x' = 5.5$ for $t' = 0$ (i.e., with its front part located slightly above the slope in order to somewhat save on the domain size). The initial BEM discretizations has 60×4 quadrilateral elements in the x- and y-directions respectively ($\Delta x'_0 = 0.30$ and $\Delta y'_0 = 0.50$), on the bottom and free surface boundaries. The lateral boundaries Γ_{r2} have grid lines connecting the free surface and bottom edge nodes, with four elements specified in the vertical direction along each pair of connecting lines. The total number of nodes in the NWT is $N_\Gamma = 1270$ and the number of quadrilateral MII elements is $M_\Gamma = 992$. The initial time step is set to $\Delta t'_0 = 0.14$ ($\mathscr{C}_0 = 0.47$).

Figure 8 presents results of computations after 122 time steps, at $t' = 7.551$. At this time, numerical errors on wave mass and energy conservation are quite small, with $\varepsilon_m = 0.056$ per cent and $\varepsilon_e = 0.117$ per cent. Due to node convergence at the wave crest, according to Equation (68), the time step has reduced to $\Delta t' = 0.0259$. The wave has shoaled up the slope and propagated to the right of the NWT; its front face reaches an almost vertical tangent at the

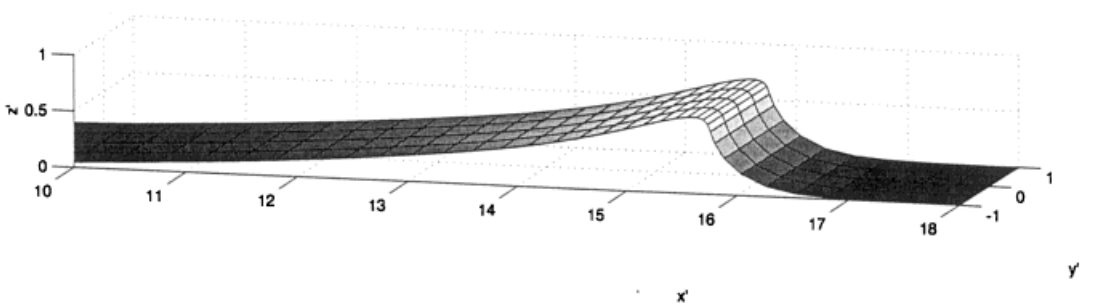

Figure 8. Shoaling of an exact solitary wave of initial height $H'_0 = 0.6$ over a 1:15 slope (Figure 7). Free surface elevation calculated at $t' = 7.551$. The wave crest is located at $x' = 5.5$ for $t' = 0$. The grid shows the BEM discretization with 60×4 quadrilateral elements on the free surface ($\Delta x'_0 = 0.3$ and $\Delta y'_0 = 0.5$).

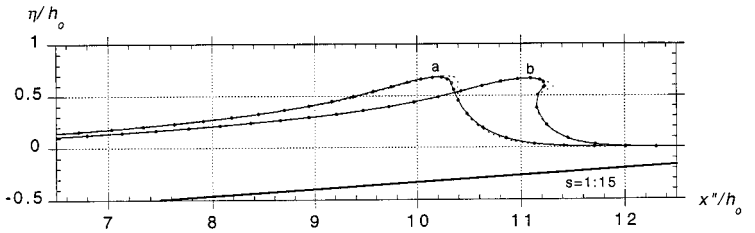

Figure 9. Comparison of three-dimensional (— ○ —) and two-dimensional (---) results [6] for the shoaling of a solitary wave of height $H'_0 = 0.6$ over a slope $s = 1{:}15$. With $x'' = x' - x'_1$ (Figure 7) and times $t' =$ (a) 7.551 (as in Figure 8) and (b) 8.163 (as in Figure 10).

crest, with $H' = 0.679$ at $x' = 15.64$. For a given x', results are identical within four significant figures for nodes in the y-direction.

Figure 9 presents a comparison of a vertical cross-section in the three-dimensional results, at $y' = 0$ (horizontally shifted to $x'' = x' - x'_1$), with two-dimensional results calculated by Grilli *et al.* [6]. Curve (a) is the same case as in Figure 8 and corresponds to the break point in the two-dimensional model, i.e., a vertical tangent on the front face. The agreement between three- and two-dimensional results is quite good for curve (a), except at the tip of the crest. This is despite the coarser discretization in the 3D-NWT, which has a resolution about two times less in the x-direction than in two-dimensional calculations. This lower resolution implies that the wave crest is less resolved in three-dimensional calculations and hence leads to the observed discrepancies.

Computations can be pursued slightly further than the stage of curve (a) with sufficient accuracy. Figure 10 shows the wave computed after 154 time steps of propagation; at $t' = 8.163$ the wave crest starts overturning. At this stage, errors on wave mass and energy conservation are still small, with $\varepsilon_m = 0.106$ per cent and $\varepsilon_e = 0.351$ per cent, and the time step has reduced to $\Delta t' = 0.0085$. Figure 9 curve (b) shows the cross-section of these results at $y' = 0$; two-dimensional results are again shown for comparison. Despite the lower resolution,

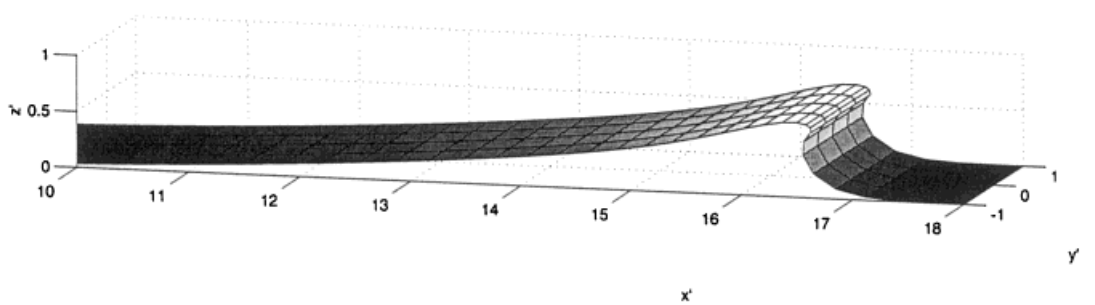

Figure 10. Same case as Figure 8. Free surface elevation calculated at $t' = 8.163$.

the agreement of three- and two-dimensional results is still good for this overturning wave. Beyond the stage of Figure 10, however, three-dimensional computations quickly fail as elements start overlapping on the lateral vertical boundaries at $y' = \pm 1$. This limitation could be eliminated by implementing appropriate regridding techniques for the elements on the sidewalls of the NWT.

3.3. Solitary wave shoaling over a sloping ridge

3.3.1. Lateral speed of propagation of wave overturning. Earlier applications were three-dimensional but showed no variation of results in the y-direction due to the y-homogeneous bottom topography. A three-dimensional overturning wave is now produced in a wider NWT of width $4h_0$ in the y-direction, having a sloping ridge at its extremity. The ridge starts at $x' = 5.225$ and has a 1:15 slope in the middle ($y = 0$), tapered in the y-direction by specifying a depth variation proportional to $\mathrm{sech}^2(ky)$ (Figure 11). The ridge is truncated at $x' = 19$, where the minimum depth is $h' = 0.093$ in the middle part ($y' = 0$) and the maximum depth is $h' = 0.619$ on the sides ($y' = \pm 2$, for $k = 0.5$), which corresponds to a 1:36 minimum slope. The initial wave is the same the 'Tanaka' solitary wave as before, with $H'_0 = 0.6$, and its crest is initially located at $x' = 5.7$ for $t' = 0$.

A coarse initial BEM discretization is selected for the bottom and free surface, with 40×8 quadrilateral elements in the x- and y-directions respectively ($\Delta x'_0 = 0.475$ and $\Delta y'_0 = 0.50$; see grids shown in Figures 11 and 12). The lateral boundaries have grid lines connecting the free surface and bottom edge nodes, with four elements specified in the vertical direction along each pair of connecting lines. The total number of nodes in the NWT for this case is $N_\Gamma = 1238$ and the number of quadrilateral MII elements is $M_\Gamma = 1024$ (600 s of CPU per time step on the G3-266). The initial time step is set to $\Delta t'_0 = 0.214$ ($\mathscr{C}_0 = 0.45$).

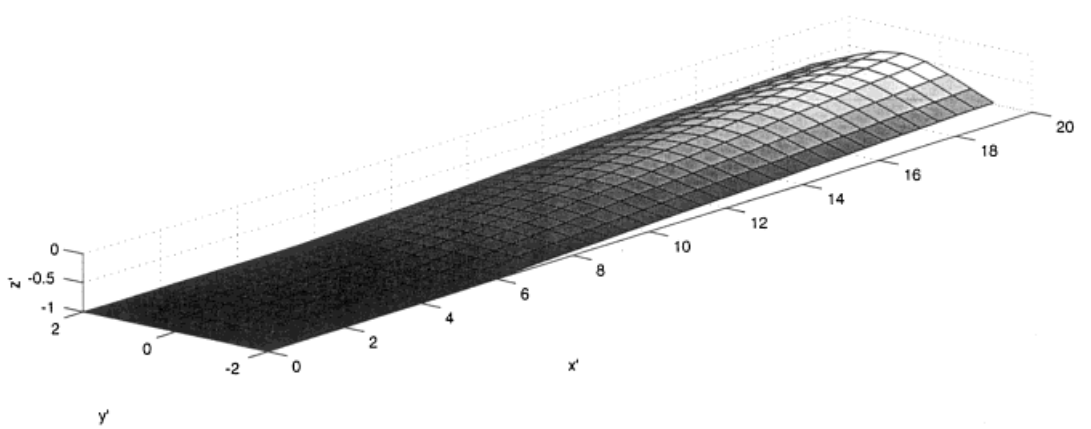

Figure 11. Bottom topography and its BEM discretization for the shoaling of a solitary wave over a ridge modeled as a sloping bottom $s = 1{:}15$, with a lateral $\mathrm{sech}^2(ky)$ modulation ($k = 0.5$ in this figure). The grid shows a BEM discretization on the bottom, with 40×8 quadrilateral elements ($\Delta x'_0 = 0.475$ and $\Delta y'_0 = 0.50$).

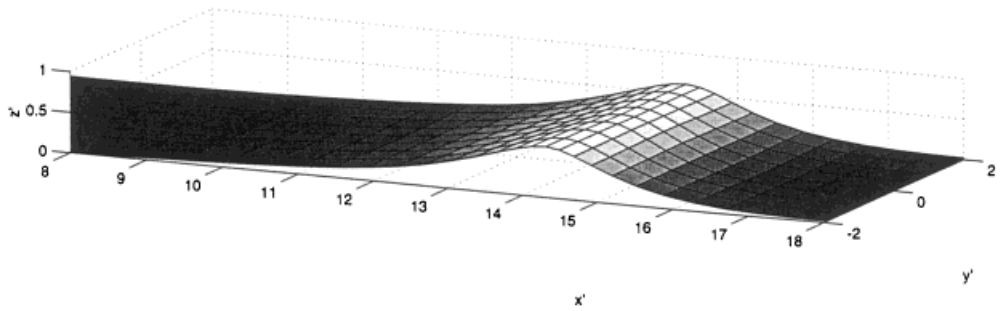

Figure 12. Free surface shape at $t' = 6.00$ for the propagation of an exact solitary wave of height $H'_0 = 0.6$ over a ridge (see Figure 11) in a 3D-NWT with 40×8 quadrilateral elements on the free surface (initial discretization). The wave crest is located at $x' = 5.7$ for $t' = 0$.

In this application, wave overturning eventually occurs and leads to a large increase in numerical errors, due to the strong convergence of nodes and the gradual loss of accuracy of numerical integrations in the overturning jet. (This is similar to results obtained in the 2D-NWT by Grilli and Subramanya [22].) In the analyses, results will be deemed acceptable when numerical errors are less than 1 per cent. Computations will first be performed in the initial discretization up to reaching these maximum errors ($t' \leq 8.788$). To refine the BEM discretization resolution in the region where wave overturning occurs, without an unnecessary large increase in the total number of nodes, regridding of the extremity of the NWT to a finer discretization will be performed for results obtained at an earlier time, when errors are very small ($t' = 6.000$) and computations restarted up to again reaching the maximum errors.

Figure 12 shows results of computations in the initial discretization after 51 time steps, at $t' = 6.000$, corresponding to the stage at which regridding is specified. At this time, numerical errors on wave mass and energy conservation are quite small, with $\varepsilon_m = 0.065$ per cent and $\varepsilon_e = 0.045$ per cent. Figure 13 shows results obtained after 103 time steps in the same discretization ($t' = 8.788$). At this time, numerical errors are $\varepsilon_m = 0.248$ per cent and $\varepsilon_e = 0.865$ per cent, i.e., close to the admissible maximum value for the latter one. Due to the node convergence at the wave crest, the time step has reduced to $\Delta t' = 0.0096$. The wave has propagated to the far right of the NWT, and its front part starts overturning in the middle shallower part of the tank ($y' = 0$), with $H' = 0.700$ at $x' = 17.010$.

Regridding is applied at $t' = 6.000$, when the wave crest is located at $x' = 14.203$ and $H' = 0.644$, i.e., much before the wave starts overturning (Figure 12). The discretization is increased to 40×10 quadrilateral elements on the free surface and bottom boundaries, for $x' = 8.075$–19, and nodes are regridded to constant intervals (with $\Delta x'_0 = 0.273$ and $\Delta y'_0 = 0.40$). The total number of nodes in the NWT is now $N_\Gamma = 1422$ and the number of quadrilateral MII elements is $M_\Gamma = 1200$ (735 s of CPU per time step on the G3-266). The initial time step after regridding is set to $\Delta t' = 0.123$ ($\mathscr{C}_0 = 0.45$). Figure 14 shows the wave computed after 130 time steps in the regridded discretization at $t' = 9.196$; the final time step has reduced to $\Delta t' = 0.0051$. At this stage, the error on wave energy conservation reaches the

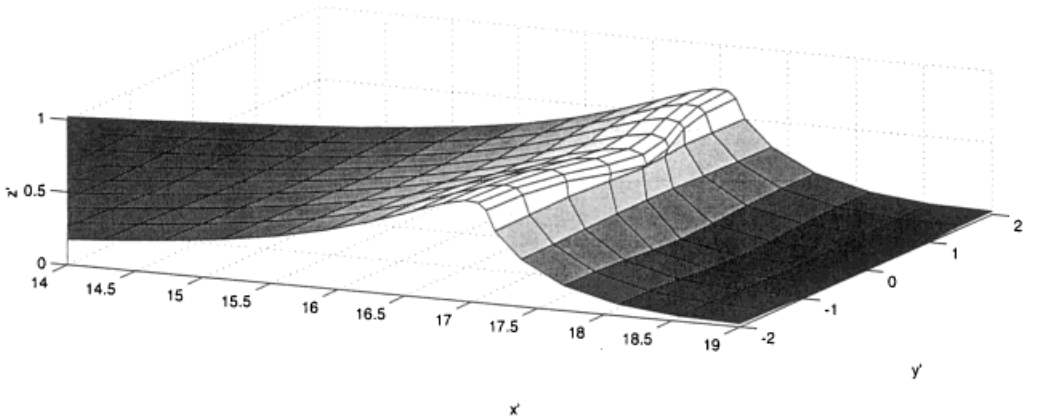

Figure 13. Same case as in Figures 11 and 12. Wave shape calculated at $t' = 8.788$ in the initial discretization (3D-NWT with 40×8 quadrilateral elements on the free surface for $x' \geq 0$).

maximum, with $\varepsilon_e = 1.012$ per cent and $\varepsilon_m = 0.164$ per cent. In fact, overturning has already reached the NWT sidewalls ($y' = \pm 2$), on which elements start wrapping; hence, computations cannot be pursued much beyond this stage. (This limitation again could be eliminated by either using proper regridding on the sidewall boundaries or by using an even wider NWT, in which wave overturning would occur for a longer time in the middle part of the wave, before reaching the sidewalls; see next application.) Comparing Figures 13 and 14 we see that by using regridding, wave overturning is both calculated for a longer time and with a finer resolution within the same maximum numerical errors.

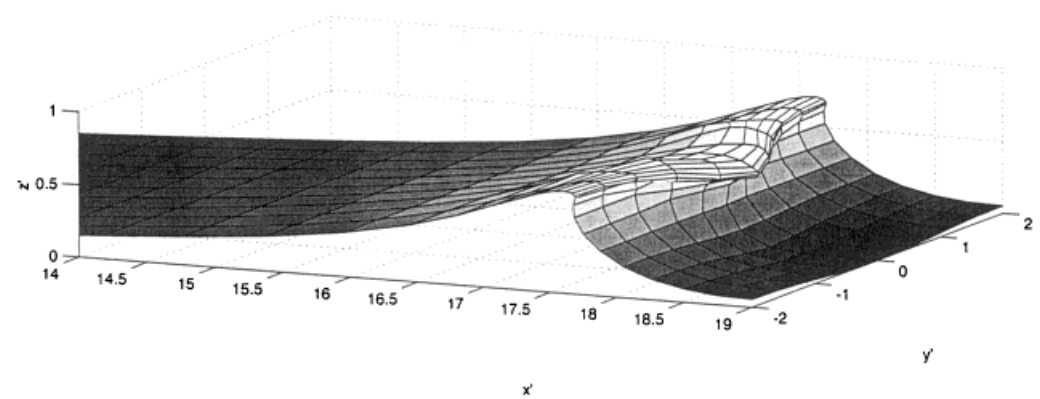

Figure 14. Same case as in Figures 11 and 12. Wave shape calculated at $t' = 9.196$ in the regridded discretization (3D-NWT with 40×10 quadrilateral elements on the free surface for $x' \geq 8.075$).

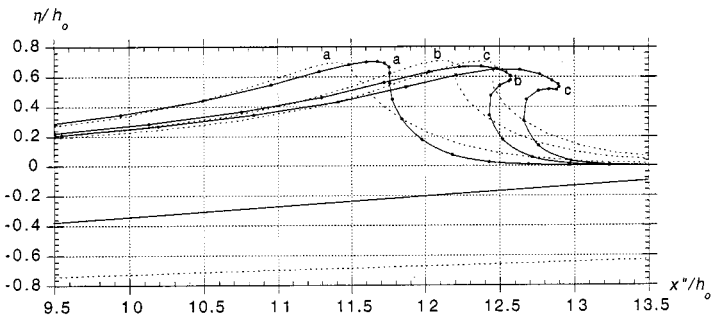

Figure 15. Vertical cross-sections shifted to $x'' = x' - x'_1$ ($x'_1 = 5.225$) at $y' = 0$ (—○—) and $y' = \pm 2$ (---) for the wave overturning over a sloping ridge, calculated in the regridded discretization with 40×10 quadrilateral elements on the free surface and bottom boundaries. Times of curves are (a) 8.485, (b) 9.005, (c) 9.196. Symbols (○) mark BEM nodes and lower straight lines show bottom cross-sections.

A problem of great scientific interest is to calculate at which speed wave overturning, i.e., breaking laterally propagates in the NWT. To do so, overturning is defined as the instant where the wave front face reaches a vertical tangent, and such occurrences are tracked in the results. Figure 15 shows results of this analysis. Curves (a) show vertical cross-sections at $y' = 0$ and $y' = \pm 2$, at the time $t' = 8.485$, when overturning first occurs in the shallower middle part of the NWT, with $H' = 0.701$ at $x' = 11.761$; the wave is still quite far from overturning along the deeper sidewalls. Curves (b) show similar results at time $t' = 9.005$, when overturning first occurs along the sidewalls, with $H' = 0.706$ at $x' = 12.199$; the wave now has a well-defined breaker jet in the middle part. Finally, curves (c) show the last computed stage of Figure 14. Using results of curves (a) and (b), we calculate $c'_b = 3.847$, as the non-dimensional lateral mean speed of propagation of the breaking front, from $y' = 0$ to ± 2.

Note that the actual boundary geometry in the BEM discretizations is much smoother than shown in Figures 11–14, where only linear interpolation was used, whereas the actual geometry is piecewise cubic.

3.3.2. Convergence of results with grid size. The previous results show that large scale three-dimensional overturning waves can be accurately calculated in the NWT. It is important, however, to also assess how such results vary as a function of the resolution of the free surface discretization, i.e., whether convergence and stability of numerical results is achieved in the NWT.

These properties were already well verified in the first application, for permanent form solitary waves over constant depth. Figure 6, for instance, shows that numerical errors on wave mass and energy decrease with a decreasing spatial step $\Delta x'_0$, i.e., an increased resolution of the discretization, when the time step is such that the Courant number is around the optimal value ($\simeq 0.45$). (Note this is also the case for all later applications due to the use of adaptive time stepping.)

A detailed analysis of result convergence and stability with grid size is now performed for a case similar to the previous application, i.e., a solitary wave of initial height $H'_0 = 0.6$ shoaling

and overturning over a sloping ridge. To delay the problem of elements wrapping on the sidewalls, a wider NWT of width $8h_0$ is used. The ridge still has a $\mathrm{sech}^2(ky)$ variation but we set $k = 0.25$, which leads to the same depth variation as before in the middle of the tank ($y' = 0$) and on the sidewalls ($y' = \pm 4$). Three discretizations are used: (a) a coarse one with $40 \times 8 \times 4$ elements in the x-, y-, and z-directions respectively, which is used for all $t' \geq 0$; (b) a medium one with $40 \times 20 \times 4$ elements, used for $t' \geq 6.05$, obtained by regridding results of discretization (a) for $x' \geq 8.075$; and (c) a finer discretization with $50 \times 20 \times 4$ elements at $t' = 0$, regridded to $60 \times 30 \times 4$ elements for $t' \geq 5.77$ and $x' \geq 8.075$. Numerical data for the three discretizations are given in Table I. Note, discretizations (a) and (b) were run on a Mac G4-450 MHz computer, using a direct solver in the BEM model, and discretization (c) was run on a CRAY-C90 computer, using an iterative solver (GMRES) and a vectorized version of the software (see Table I for CPU times).

Free surface elevations computed at $t' = 8.25$, in the three discretizations, are shown in Figure 16; at this time, maximum numerical errors are much less than 1 per cent (Table I), and free surface elevations appear smooth (despite the linear interpolation in the plotting algorithm), indicating a good stability of results. Results show that the three-dimensional breaker jet is increasingly better resolved as the discretization is increased. Computational errors on wave mass and energy are also smaller, the finer the discretization (Table I). In all three discretizations, however, errors become larger for later times and numerical instabilities eventually occur at the tip of the breaker jets when, due to flow convergence, nodes become too close to each other for the integrals to be accurately calculated (unless a prohibitive number of subdivisions is used in the adaptive integrations) and the time step becomes extremely small. Instability occurs in discretization (a) at $t' > 8.40$, (b) at $t' > 8.25$, and (c) at $t' > 8.57$ due to node convergence. In the latter case, however, numerical errors are still quite small with $\varepsilon_m = 0.017$ per cent and $\varepsilon_e = 0.42$ per cent, for $\Delta t' = 0.0034$, and Figure 17 shows the free surface computed at this stage. A finely resolved three-dimensional overturning jet can be seen on the figure.

To assess result convergence, Figure 18 compares vertical cross-sections in the results of Figure 16, for the three discretizations at $t' = 8.25$, for $y' = 0$ and $y' \pm 4$ (curves (a)). Cross-sections in final results for discretization (c) at $t' = 8.57$ (Figure 17) are also shown (curves (b)). The good convergence of results with the discretization is quite clear on the figure.

Table I. Numerical data for discretizations (a), (b), and (c) used for computing solitary wave shoaling over a ridge

Discretization (elements)	N_Γ	M_Γ	$\Delta x'_0$	$\Delta y'_0$	CPU/step	Steps	ε_m (%)	ε_e (%)	t'_f
(a) $40 \times 8 \times 4$	1238	1024	0.475	1.000	3.0′ (G4)	94	0.160	0.540	8.25
(b) $40 \times 8 \times 4$	1238	1024	0.475	1.000	3.0′ (G4)	52	0.058	0.515	6.05
(b) $40 \times 20 \times 4$	2342	2080	0.273	0.400	14.4′ (G4)	95	0.070	0.677	8.25
(c) $50 \times 20 \times 4$	2862	2560	0.380	0.400	9.4′ (CR)	70	0.012	0.035	5.77
(c) $60 \times 30 \times 4$	4702	4320	0.182	0.267	20.9′ (CR)	120	0.015	0.260	8.25

In each case $\Delta t'_0 = 0.45\Delta x'_0$; t'_f indicates the time for which maximum errors are given. G4, Mac G4-450MHz computer (132 Mb used for execution); CR, CRAY-C90 computer (829 Mb used for execution).

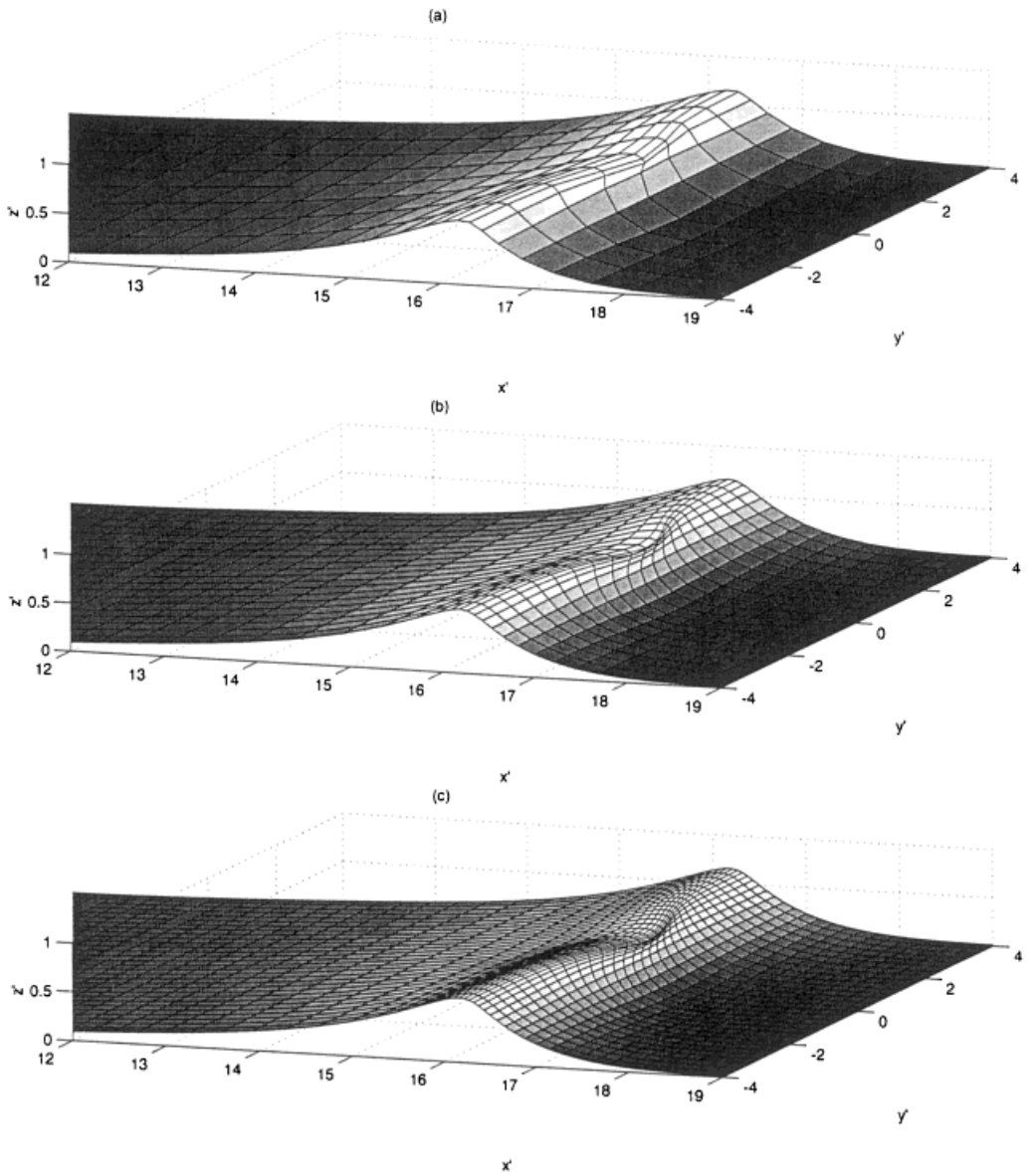

Figure 16. Free surface shape computed at $t' = 8.25$ for the propagation of an exact solitary wave of height $H'_0 = 0.6$ over a slopping ridge (see Figure 11), in the 3D-NWT with discretizations (a), (b), and (c) (Table I). The wave crest is located at $x' = 5.7$ for $t' = 0$.

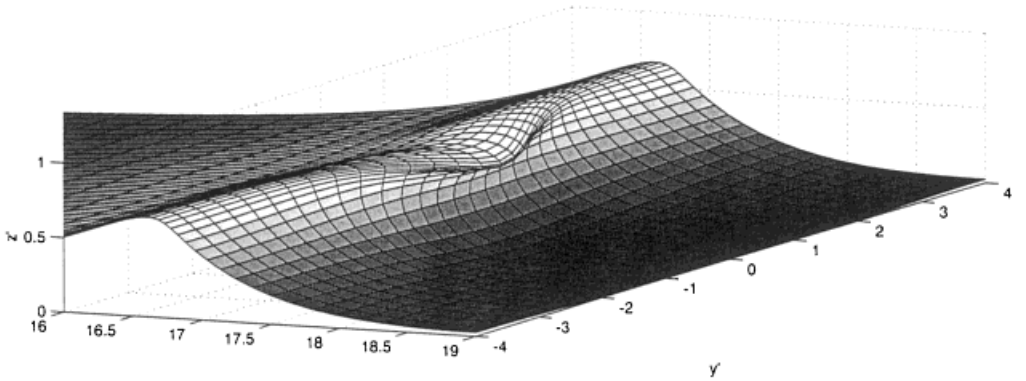

Figure 17. Same case as in Figure 16(c) at $t' = 8.57$.

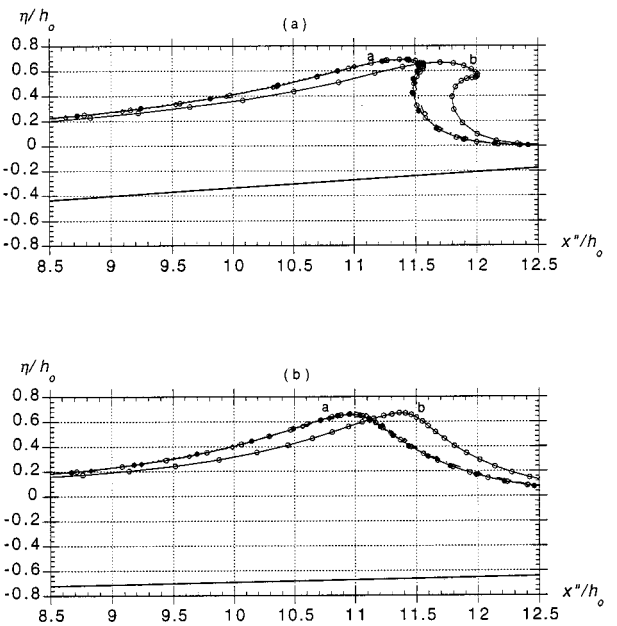

Figure 18. Same case as in Figures 16 and 17. Vertical cross-sections in surface elevations and bottom topography at $t' = 8.25$ (curves a) and $t' = 8.57$ (curves b) shifted to $x'' = x' - x'_1$ ($x'_1 = 5.225$) for (a) $y' = 0$, and (b) $y' = \pm 4$ and discretizations (Table I): (— -◇- —; a), (---●---; b), and (—○—; c). Symbols denote discretization nodes.

All results agree well with each other, particularly in the back of the wave and in the overturning jet. Even the very coarse discretization (a) is able to predict quite well the shape of the overturning wave. Curves (b) show how nodes/elements become very dense at the wave crest and in the breaker jet, eventually leading to quasi-singularities in the integrations.

4. CONCLUSIONS

An accurate and efficient 3D-NWT was developed, implemented, and tested. Overall, results obtained in this study show a better stability and numerical accuracy than in previous attempts reported in the literature of calculating such strongly non-linear three-dimensional surface waves. Large scale wave overturning over arbitrary bottom topography is calculated which, to our knowledge, was never successfully achieved in a general 3D-NWT. An interesting physical result is the speed of lateral propagation of wave breaking; this will be further investigated in future studies.

More specifically, in the reported applications, global accuracy of computations in terms of conservation of wave mass and energy is always very good and the computed wave shape converges well with the grid size, particularly in the overturning region. No numerical problems are experienced at boundary intersections (corners/edges) of the computational domain (e.g., as in Romate [34]), nor are sawtooth instabilities observed at the grid wavelength, with growing time. No smoothing is thus required to stabilize the solution (e.g., as in Xü and Yue [35,36]). When regridding is used, it is simply to introduce more nodes/fluid particles in selected areas of the free surface, to provide more resolution; the solution at the current time step is simply reinterpolated but not modified and hence this does not constitute smoothing (i.e., filtering). Different interpolation methods are used for the BEM computations and for calculating the tangential derivatives required for time stepping, but this does not constitute (explicit) smoothing either. Note only a few hundred time steps were run in the 3D-NWT for these applications, but similarly accurate and stable results were observed in Grilli *et al.*'s 2D-NWT, which is based on similar algorithms, for computations covering several thousands of time steps.

As in earlier two-dimensional applications [18,22,46], which showed similar accuracy and stability properties, we believe that the accuracy and stability of the three-dimensional model results from both the higher-order BEM method, with C_2 local inter-element continuity, which ensures a very accurate solution of Laplace's equation at every time step, and the explicit time stepping method based on second-order Taylor series, which include higher-order spatial derivatives to calculate the new position of a node at the next time step. This method had been shown in two dimensions to be more stable, accurate, and efficient than predictor–corrector methods, which simply extrapolate the position of each node, based on earlier locations on its own trajectory, without any effect of neighboring nodes (i.e., spatial variations); this more easily leads to sawtooth instabilities. We find that the same holds true for the three-dimensional model. As pointed out by Xü and Yue [36], such strongly non-linear surface wave problems require very accurate numerical methods in all respects, to prevent errors from growing in time, through non-linear interactions, and leading to the numerical instability of the solution. Here, even after almost 200 time steps (last application) no significant error is observed for mass and energy conservation, without need for smoothing the solution.

Finally, as mentioned before, these are quite demanding numerical computations. In the present study, the focus was on developing and validating the 3D-NWT and no specific attempt was made to optimize the solution for very large problems, such as dividing the domain in sub-regions (Wang *et al.* [50]), except that the more efficient GMRES iterative solver was used for the larger BEM systems of equations (as, e.g., in Xü and Yue [35,36] or Ferrant [39]) and the software code was optimized for the CRAY-C90 supercomputer. It should be pointed out, however, that with the ever increasing power of microprocessors, even problems with fairly large discretization sizes can still be run on desktop computers. For instance, many of the computations reported in this paper were performed on a laptop Mac PowerPC G3 computer (266 MHz, 64 Mb of RAM), on which the largest problem, with 1422 nodes, took about 12.25 min of CPU per time step and 49 Mb of RAM. Even larger problems were run on a Mac PowerPC G4 computer (450 MHz, 1 Gb of RAM), which turned out to be 3–4 times faster than the G3 and about half as fast as the CRAY-C90; the largest problem run on the G4 had 2342 nodes and took about 14.40 min of CPU per time step and 132 Mb of RAM. Since the computation time using the iterative solver and the NWT memory requirement both grow with the power 2 or so of the number of nodes N_Γ, it is anticipated that with the present implementation of the model a problem with 6400 nodes could be run on the G4 computer, using about 950 Mb of RAM and 105 min CPU per time step. For even larger three-dimensional problems, much more important computer resources and/or use of optimizing techniques would be required. Clearly, even with faster algorithms, such computations would require a supercomputer such as the CRAY-C90 or even a massively parallel supercomputer.

It is anticipated that a fully optimized and vectorized/parallelized 3D-NWT will make it possible to efficiently perform very large size computations, thus providing a great wealth of new insight into the physics of three-dimensional breaking waves.

ACKNOWLEDGMENTS

This publication is the result of research sponsored by the 'Centre National de la Recherche Scientifique' (CNRS, France). Support to the first author, provided by the Institut Non-Linéaire de Nice, UMR 6618 CNRS-UNSA, while he was on sabbatical leave in France, is gratefully acknowledged, as well as a grant from the US Office of Naval Research (N-00014-99-10439 of the Coastal Dynamics Division; code 321 CD). The second and third authors acknowledge support from the Délégation Générale de l'Armement. The computations presented in this work were performed in part on the CRAY-C90 supercomputer located at IDRIS (Institut du Développement et des Resources en Informatique Scientifique, France), and were funded by the CNRS.

REFERENCES

1. Mei CC. *The Applied Dynamics of Ocean Surface Waves* (2nd edn). World Scientific: New Jersey, 1989.
2. Wei J, Kirby JT, Grilli ST, Subramanya R. A fully nonlinear Boussinesq model for surface waves. I. Highly nonlinear unsteady waves. *Journal of Fluid Mechanics* 1995; **294**: 71–92.
3. Dommermuth DG, Yue DKP, Lin WM, Rapp RJ, Chan ES, Melville WK. Deep-water plunging breakers: a comparison between potential theory and experiments. *Journal of Fluid Mechanics* 1988; **189**: 423–442.
4. Skyner D. A comparison of numerical predictions and experimental measurements of the internal kinematics of a deep-water plunging wave. *Journal of Fluid Mechanics* 1996; **315**: 51.

5. Grilli ST, Subramanya R, Svendsen IA, Veeramony J. Shoaling of solitary waves on plane beaches. *Journal of Waterways, Port, Coastal and Ocean Engineering* 1994; **120**(6): 609–628.
6. Grilli ST, Svendsen IA, Subramanya R. Breaking criterion and characteristics for solitary waves on plane beaches. *Journal of Waterways, Port, Coastal and Ocean Engineering* 1997; **123**(3): 102–112.
7. Li Y, Raichlen F. Breaking criterion and characteristics for solitary waves on slopes—Discussion. *Journal of Waterways, Port, Coastal and Ocean Engineering* 1998; **124**(6): 329–333.
8. Grilli ST. Free surface nonlinear flows. In *1999 McGraw-Hill Yearbook of Sciences and Technology* (a yearly supplement to the *Encyclopedia of Sciences and Technology*), Parker SP (ed.). McGraw-Hill: New York, 1997; 134–136.
9. Guignard S, Marcer R, Rey V, Kharif C, Fraunié Ph. Solitary wave breaking on sloping beaches: 2D two-phase flow numerical simulation by SL-VOF method. *European Journal of Mechanics B/Fluids* 2001 (accepted).
10. Chen G, Kharif C, Zaleski S, Li J. Two-dimensional Navier–Stokes simulation of breaking waves. *Physics and Fluids* 1999; **111**: 121–133.
11. Guignard S, Grilli ST, Marcer R, Rey V. Computation of shoaling and breaking waves in nearshore areas by the coupling of BEM and VOF methods. In *Proceedings of the 9th International Offshore and Polar Engineering Conference (ISOPE99)*, Brest, France, May, vol. III, Chung JS, Olagnon M, Kim CH, Francescutto A (eds). International Society of Offshore and Polar Engineers: Cupertino 1999; 304–309.
12. Brebbia CA. *The Boundary Element Method for Engineers*. Wiley: New York, 1978.
13. Longuet-Higgins MS, Cokelet ED. The deformation of steep surface waves on water—I. A numerical method of computation. *Proceedings of the Royal Society London* 1976; **A350**: 1–26.
14. Dold JW, Peregrine DH. An efficient boundary integral method for steep unsteady water waves. In *Numerical Methods for Fluid Dynamics II*, Morton KW, Baines MJ (eds). Clarendon Press: Oxford, 1986; 671–679.
15. Vinje T, Brevig P. Numerical simulation of breaking waves. *Advances in Water Research* 1981; **4**: 77–82.
16. New AL, McIver P, Peregrine DH. Computation of overturning waves. *Journal of Fluid Mechanics* 1985; **150**: 233–251.
17. Klopman G. Numerical simulation of gravity wave motion on steep slopes. Delft Hydraulics Report No. H195, 1988.
18. Grilli ST, Skourup J, Svendsen IA. An efficient boundary element method for nonlinear water waves. *Engineering Analysis with Boundary Elements* 1989; **6**(2): 97–107.
19. Cointe R. Numerical simulation of a wave channel. *Engineering Analysis with Boundary Elements* 1990; **7**(4): 167–177.
20. Cooker MJ. A boundary-integral method for water wave motion over irregular bed. *Engineering Analysis with Boundary Elements* 1990; **7**(4): 205–213.
21. Ohyama T, Nadaoka K. Development of a numerical wave tank for analysis of nonlinear and irregular wave fields. *Fluid Dynamics Research* 1991; **8**: 231–251.
22. Grilli ST, Subramanya R. Numerical modeling of wave breaking induced by fixed or moving boundaries. *Computational Mechanics* 1996; **17**: 374–391.
23. Grilli ST, Horrillo J. Numerical generation and absorption of fully nonlinear periodic waves. *Journal of Engineering Mechanics* 1997; **123**(10): 1060–1069.
24. Dommermuth DG, Yue DKP. Numerical simulation of nonlinear axisymmetric flows with a free surface. *Journal of Fluid Mechanic* 1987; **178**: 195–219.
25. Forbes LK. An algorithm for three-dimensional free-surface problems in hydrodynamics. *Journal of Computational Physics* 1989; **82**(2): 330–347.
26. Boo SY. Application of higher-order boundary element method to steady ship wave problem and time domain simulation of nonlinear gravity waves. PhD dissertation, Ocean Engineering Progress, Texas A&M University, 1993.
27. Lee CC, Liu YH, Kim CH. Simulation of nonlinear waves and forces due to transient and steady motion of a submerged sphere. *International Journal of Offshore and Polar Engineering* 1994; **4**(3): 174–182.
28. Isaacson M, de St. Q. Nonlinear effects on fixed and floating bodies. *Journal of Fluid Mechanics* 1982; **120**: 267–281.
29. Yang C, Ertekin RC. Numerical simulation of nonlinear wave diffraction by a vertical cylinder. *Journal of Offshore Mechanics and Arctic Engineering* 1992; **114**: 36–44.
30. Cheung KF, Isaacson M, Lee JW. Wave diffraction around a three-dimensional body in a current. *Journal of Offshore Mechanics and Arctic Engineering* 1996; **118**(4): 247–252.
31. Lalli F, Di Mascio A, Landrini M. Nonlinear diffraction effects around a surface-piercing structure. *International Journal of Offshore and Polar Engineering* 1996; **6**(2): 104–111.
32. Celebi MS, Kim MH, Beck RF. Fully nonlinear 3D numerical wave tank simulations. *Journal of Ship Research* 1998; **42**(1): 33–45.

33. Ferrant P. Runup on a cylinder due to waves and currents: potential flow solution with fully nonlinear boundary conditions. In *Proceedings of the 8th International Offshore and Polar Engineering Conference*, Montreal, vol. 3, Chung JS, Olagnon M, Kim CH, Koterayama W (eds). International Society of Offshore and Polar Engineers: Cupertino, 1998; 332–339.
34. Romate JE. The numerical simulation of nonlinear gravity waves in three dimensions using a higher order panel method. PhD dissertation, Department of Applied Mathematics, University of Twente, The Netherlands, 1989.
35. Xü H, Yue DKP. Numerical study of three dimensional overturning waves. In *Proceedings of the 7th International Workshop on Water Waves and Floating Bodies*, Cointe R (ed.). Val de Reuil, France, May, Fluid Flow and Computational Aspects, 1992; 303–307.
36. Xü H, Yue DKP. Computations of fully-nonlinear three-dimensional water waves. In *Proceedings of the 19th Symposium on Naval Hydrodynamics*, Seoul, Korea, August, 1992.
37. Broeze J. Numerical modelling of nonlinear free surface waves with a 3D panel method. PhD dissertation, Enschede, The Netherlands, 1993.
38. Boo SY, Kim CH, Kim MH. A numerical wave tank for nonlinear irregular waves by 3D higher-order boundary element method. *International Journal of Offshore and Polar Engineering* 1994; **4**(4): 265–272.
39. Ferrant P. Time domain computation of nonlinear diffraction loads upon three-dimensional floating bodies. In *Proceedings of the 5th International Offshore and Polar Engineering Conference*, The Hague, vol. 3, Chung JS, Olagnon M, Koterayama W (eds). International Society of Offshore and Polar Engineers: Cupertino, 1995; 280–288.
40. Yeung RW. Numerical methods in free surface flows. *Annual Review in Fluid Mechanics* 1982; **14**: 395–442.
41. Peregrine DH. Breaking waves on beaches. *Annual Review of Fluid Mechanics* 1983; **15**: 149–178.
42. Grilli ST. Modeling of nonlinear wave motion in shallow water. In *Computational Methods for Free and Moving Boundary Problems in Heat and Fluid Flow*, Wrobel LC, Brebbia CA (eds). Computational Mechanics Publisher, Elsevier Applied Science: London, 1993; 37–65.
43. Grilli ST, Subramanya R. Recent advances in the BEM modelling of nonlinear water waves. In *Boundary Element Applications in Fluid Mechanics. Advances in Fluid Mechanics Series*, Power H (ed.). Computational Mechanics Publishers: Southampton, 1995; 91–122.
44. Tsai WT, Yue DKP. Computation of nonlinear free-surface flows. *Annual Review of Fluid Mechanics* 1996; **28**: 249–278.
45. Kim CH, Clément AH, Tanizawa K. Recent research and development of numerical wave tank—a review. *International Journal of Offshore and Polar Engineering* 1999; **9**(4): 241–256.
46. Grilli ST, Svendsen IA. Corner problems and global accuracy in the boundary element solution of nonlinear wave flows. *Engineering Analysis with Boundary Elements* 1990; **7**(4): 178–195.
47. Grilli ST, Subramanya R. Quasi-singular integrals in the modeling of nonlinear water waves in shallow water. *Engineering Analysis with Boundary Elements* 1994; **13**(2): 181–191.
48. Badmus T, Cheng AH-D, Grilli ST. A three-dimensional Laplace transform BEM for poroelasticity. *International Journal for Numerical Methods in Engineering* 1993; **36**: 67–85.
49. Tanaka M. The stability of solitary waves. *Physics and Fluids* 1986; **29**(3): 650–655.
50. Wang P, Yao Y, Tulin MP. An efficient numerical tank for nonlinear water waves based on the multi-subdomain approach with BEM. *International Journal of Numerical Methods in Fluids* 1995; **20**: 1315–1336.

